Numerical Modeling of Wave Propagation at Large Scale Damaged Structures For Quantitative AE

BY

ZAHRA HEIDARY
B.A. (University of Shahid Bahonar, Iran) 2005

THESIS

Submitted in partial fulfillment of the requirements
for the degree of Doctor of Philosophy in Civil Engineering
in the Graduate College of the
University of Illinois at Chicago, 2014

Chicago, Illinois

Defense Committee:

Dr. Didem Ozevin, Chair and Advisor
Dr. J. Ernesto Indacochea, Civil & Materials Engineering
Dr. Craig D. Foster, Civil & Materials Engineering
Dr. Michael J. McNallan, Civil & Materials Engineering
Dr. Ahmed A. Shabana, Mechanical &Industrial Engineering

This thesis is dedicated

to my brilliant and supportive husband

for his remarkable patience during the challenges of graduate study.

ACKNOWLEDGMENTS

First and foremost I want to thank my advisor Didem Ozevin, for her immense knowledge, warm encouragement, and thoughtful guidance. I have been extremely lucky to have an advisor who gave me the freedom to research on my own and the guidance when I needed. It has been an honor to be her first Ph.D. student. I am thankful for all her contributions of time, knowledge, and funding to make my Ph.D. experience the one that I will cherish forever. I am also thankful for the fantastic example she has provided as a successful woman professor. I would like to express my sincere gratitude to my thesis committee: Prof. J. Ernesto Indacochea, Prof. Michael J. McNallan, Prof. Ahmed Shabana, and Prof. Craig D. Foster, for their encouragement, insightful comments, and hard questions.

Completing this thesis would ha

ve been not possible without the support provided by the other members of Non-Destructive Evaluation lab. Many thanks to James, Hazim, Mr. Fazel, Minoo, Maryam, Zeynab, Amir, and Lu for helping me enrich my ideas and stimulating discussions. I greatly cherish their friendship and I sincerely appreciate their belief in me. I also want to thank my immediate and extended family for their genuine love and encouragement. Most importantly, I want to thank my loving and caring husband who has been constant source of love, inspiration, and support all these years. I owe everything to him.

CONTRIBUTION OF AUTHORS

This thesis is comprised of seven chapters. Following the introductory chapter (chapter 1) which sketch the problem in hand and the approach taken to resolve it, chapter 2 includes literature pertinent to the subject of this research, including the AE method, numerical formulation of wave propagation using classical finite element and spectral element methods, and the challenges of using finite elements approach with the AE method. This chapter (chapter 2) has been previously partially used in published conferences proceedings [1], [2] with my research advisor, Dr. Ozevin, as the co-author. Chapter 3 presents the theory of the spectral element formulation. The accuracy and efficiency of the SEM formulation in comparison to conventional finite element formulation are discussed. The content presented in the chapter 3 was previously partially published in a conference proceeding [1]. Chapter 4 which was published as a journal article [3] with my research advisor, Dr. Ozevin, as the co-author, describes a novel method developed to study the wave propagation in long-range pipe structures, using spectral elements and the partitioning method of the strain-displacement matrix. Numerical formulations are validated using COMSOL Multiphysics and ANSYS software. The following chapter (Chapter 5) which was previously partially published in a conference proceeding [2] is concerned with modeling of unbounded domains. The methodology and finite element implementation of absorbing boundary condition are discussed. The accuracy of the numerical formulation is then validated by the experimental results. The influence of reflected waves on the received elastic wave characteristics is discussed. Chapter 6, which was previously partially published in a

CONTRIBUTION OF AUTHORS (Continued)

conference proceeding [2], presents multi-physics models including piezoelectric and structural mechanics to study the influence of piezoelectric transducers on the wave motion. Finally, conclusions and future work are discussed in chapter 7. Appendix A was also partially presented in a conference proceeding [2].

TABLE OF CONTENTS

TABLE OF CONTENTS (Continued)

CHAPTER **PAGE**

LIST OF TABLES

LIST OF FIGURES

LIST OF FIGURES (Continued)

FIGURE **PAGE**

SUMMARY

The content of this chapter was previously partially published as "Efficient computation of wave propagation along axisymmetric pipes under non-axisymmetric loading" in the journal of "Finite Elements in Analysis and Design" with my research advisor, Dr. Ozevin, as the co-author [3], also in the proceeding of the SPIE 2013 conference of Smart Structures/NDE as "The selection of spectral element polynomial orders for high frequency numerical wave propagation" with my research advisor Dr. Ozevin as the co-author [1], and also in the proceeding of the SPIE 2014 conference of Smart Structures/NDE as "High frequency elastic wave propagation in large structures using spectral elements and perfectly matched layer" with my research advisor, Dr. Ozevin, as the co-author [2].

The goal of this study is to understand the quantitative significance of propagating elastic waves released by newly formed damage surfaces through effective finite element models combining the components of source, structure and sensor into the model. The Acoustic Emission (AE) method is a nondestructive testing method that relies on the waves emitted from localized permanent deformation. The complexity of the AE method leads to qualitative understanding of damage instead of quantitative features (e.g., damage mode, size, direction). The central hypothesis of the research is that a finite element formulation using spectral elements together with absorbing boundary conditions (perfectly matched layer) reduces the finite element calculation of wave propagation in materials to such a level that the AE method will be altered from qualitative to quantitative for various practical applications. In addition to the modeling of the

propagating medium, the transfer function of the AE sensor (typically piezoelectric) is coupled with the solid model using multi-physics simulations to obtain the electrical displacement of the sensor under given excitation.

In this study, a detailed investigation of spectral element formulation for different Legendre polynomial orders and frequency resolutions is performed on the elastodynamic problem of an isotropic plate. The node per wavelength value can be used for identifying the polynomial order and the element size. Erroneous waveforms due to insufficient node per wavelength ratio are demonstrated with incorrect wave velocity, wave amplitude, and spurious wave motions. The critical element sizes for different polynomial orders are identified. An application of spectral element formulation to study wave propagation in long-range pipelines is presented. An efficient formulation of the problem of wave propagation along the length of axisymmetric pipes under non-axisymmetric loading such as leaks or new cracks is developed such that wave characteristics in a long-range pipe can be identified without the excessive computational time associated with most current 3D modeling techniques. The axisymmetric geometry of the pipe is simplified by reducing the problem to 2D while the non-axisymmetric loading is represented by the summation of Fourier series. The strain-displacement matrix is partitioned in such a way that numerical integration components are decoupled from θ (the angular parameter) and n (the Fourier series terms). The numerical formulation is built using spectral elements. The orthogonal Legendre polynomials are selected to define the nodal points of the discretized finite element. The 2D numerical model is compared with the 3D model using conventional finite element software, and the accuracy of the 2D model is validated under static and dynamic loading.

Because the numerical integration elements of the stiffness matrix are independent from θ and n, and the diagonal mass matrix resulting from the use of spectral elements, long pipes could be modeled for high frequency wave propagation. In order to investigate the influence of boundary reflections to the elastic wave properties at the receiving points, the displacement-based time-domain PMLs along with the spectral element formulations are studied. The influence of boundary reflections on the received signals, which makes the application of small coupon specimen results to large scale structures questionable, is discussed. The complexity of recording the AE signals related to the propagating wave medium and the sensing element is investigated. As the boundary reflections and the piezoelectric sensor selected in testing modify the output signal significantly, the repeatability of the AE results from one test condition to another becomes a challenge. The changes in structural geometry or sensor type vary the output signal characteristics such that the damage patterns obtained from a specific test condition cannot be repeated in another test condition. The numerical models offer a significant potential to tackle the problem of the repeatability. If the sample size is selected appropriately based on the target frequency of interest and the reflected waves are eliminated from the waveform windows, adapting the scaled experimental results to other structures becomes feasible. Complete numerical modeling including the propagating medium to the piezoelectric sensor is needed for quantitative AE.

CHAPTER 1

INTRODUCTION

1.1 Motivation

Acoustic Emission (AE) is a passive nondestructive testing (NDT) method that relies on the propagating elastic waves initiated by newly formed damage surfaces. The acoustic emission technique can be used to identify events that lead to failure of the material using sensors coupled to the surface of the material. When a structure is subjected to an external stimulus (change in pressure, load, or temperature), localized sources trigger the release of energy, in the form of elastic waves, which propagate to the surface and are detected by the AE sensors. Typical examples of damage mechanisms detected using the AE method are crack growth for isotropic materials, and fiber breakage and matrix debonding for composites. The method can be implemented for global or local damage detection for short-term or continuous monitoring. This method is relatively inexpensive, since it only requires a few sensors to be mounted at strategic locations to provide health monitoring of a structure, including locations that are difficult to access by more localized techniques such as ultrasonic inspection. The method can locate and characterize the damage after certain signal processing approaches. Unfortunately, the AE method is not being used to its full advantage because of a problem in detecting the induced micro-damage signals which can be obscured by mechanical noise. Additionally, conventional AE sensors are resonant-type piezoelectric sensors, which modify the surface mo-

tion significantly. The correlation between the AE signature and the damage source becomes more difficult. Therefore, an approach to understand the characteristics of elastic waves due to damage mechanisms in a structure is needed for better source and noise discrimination and to develop a quantitative understanding of damage (e.g. type, orientation) based on the AE measurement. One option is to conduct laboratory testing; however, for large scale structures, it is not feasible to simulate the field condition in a laboratory system. The influence of boundaries on propagating waves prevent the direct use of the results detected by the AE sensors for small-scale coupons to predict the result in large scale structures. The ability to accurately model elastic waves offers significant potential for differentiating noise and improving the interpretation of AE data [4]. In addition to understanding frequency content of elastic waves due to damage mechanisms, the models can be used to identify the optimal sensor placement and the scaling of laboratory tests to large structures as in real life applications. The analytical solutions for wave propagation are limited to simple geometries [5]. Numerical methods (e.g. Finite Element) are needed to understand the wave propagation phenomena in complex geometries. The overall hypothesis of this research is that if numerical methods are properly utilized to provide a quantitatively accurate signature of damage and the source is identified with fracture models, then the data acquisition system can be programmed to recognize this signature in the midst of background noise. If successful, this enhancement to traditional AE will transform the practice of damage detection by providing efficient real-time continuous monitoring of the safety of civil structures.

1.2 Objectives

1.2.1 Objective of the Research

The goal of this research is to understand the quantitative significance of the AE signatures through effective finite element models combining the components of source, structure and sensor into the model. The central hypothesis is that the finite element formulation using spectral elements together with absorbing boundary conditions (perfectly matched layer) will reduce the finite element calculation of wave propagation in large scale structures to such a level that the AE method will be altered from qualitative to quantitative for various practical applications. Figure 1 shows an example of large scale structure with sub-model utilizing Absorbong Boundary Condition (ab,bc,cd,da) and the sensors into the model. The transfer function of the AE sensor (typically piezoelectric) is coupled with the solid model to obtain the electrical displacement of the sensor under given excitation and understand the influence of the sensor response to the output signal.

1.2.2 Summary of Approach

The research involves five tasks:

- Perform a literature review on AE, wave propagation, quantitative analysis, spectral finite element method (SEM) and absorbing numerical boundary layers;
- Develop a finite element design to reduce the required number of elements to achieve 400 kHz frequency resolution with a reasonable mesh size;

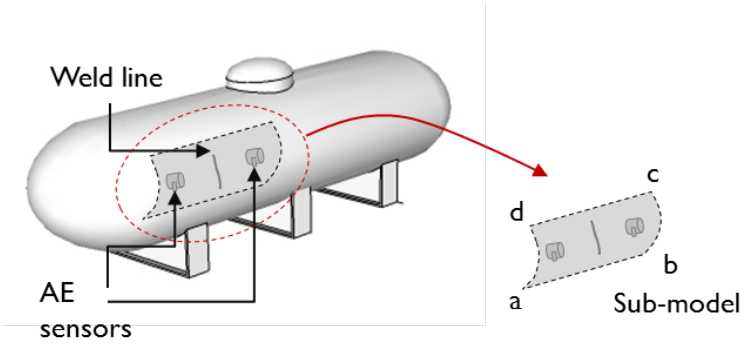

Figure 1: Sub-model approach to study wave propagation in a large scale structure

- Identify the boundary domain variables for eliminating reflections from sub-domain formulation of the structure;
- Implement the transfer function of the piezoelectric sensors into the model;
- Validate the formulation with the conventional approach and an experimental program.

1.3 Contribution to Knowledge

The major contribuations of this research are:

- The selection of polynomial order and element size for the spectral element formulation of high frequency elastodynamic problems;
- An efficient formulation of the wave propagation problem in axisymmetric pipes under non-axisymmetric loading using spectral elements and a strain-displacement partitioning approach;

- A wavelength-based model for selecting the size of the coupon sample in order to reduce the influence of boundary reflections for translating the coupon data to larger scale geometries;
- Definite understanding of piezoelectric sensor distortion of the wave motion for quantitative acoustic emission.

1.4 Organization of Dissertaion

This thesis is comprised of seven chapters. Following this introductory chapter, Chapter 2 includes literature pertinent to the subject of this research, including the AE method, numerical formulation of wave propagation using classical finite element and spectral element methods, and the challenges of using finite elements approach with the AE method. Chapter 3 presents the theory of the spectral element formulation. The accuracy and efficiency of the SEM formulation in comparison to conventional finite element formulation are discussed. Chapter 4 describes a novel method developed to study the wave propagation in long-range pipe structures, using spectral elements and the partitioning method of the strain-displacement matrix. Numerical formulations are validated using COMSOL Multiphysics and ANSYS software. The following chapter (Chapter 5) is concerned with modeling of unbounded domains. The methodology and finite element implementation of absorbing boundary condition are discussed. The accuracy of the numerical formulation is then validated by the experimental results. The influence of reflected waves on the received elastic wave characteristics are discussed. Chapter 6 presents multi-physics models including piezoelectric and structural mechanics to study the

influence of piezoelectric transducers on the wave motion. Finally, conclusions and future work are discussed in chapter 7.

CHAPTER 2

BACKGROUND

The content presented in this chapter was previously partially published in the proceeding of the SPIE 2013 conference of Smart Structures/NDE as "The selection of spectral element polynomial orders for high frequency numerical wave propagation" with my research advisor Dr. Ozevin as the co-author [1], also in the proceeding of the SPIE 2014 conference of Smart Structures/NDE as "High frequency elastic wave propagation in large structures using spectral elements and perfectly matched layer" with my research advisor, Dr. Ozevin, as the co-author [2].

2.1 Introduction

This chapter begins with relevant background information regarding real time Structural Health Monitoring (SHM) of aging structures, followed by a brief description of the acoustic emission (AE) method. Current approaches to the quantitative AE method and existing challenges pertinent to laboratory-scale results are discussed. The general solution of the elastodynamic wave equation is presented. An approach that combines the spectral element method (SEM) and absorbing boundary condition (ABC) to solve the wave equation numerically for high frequency wave propagation in large scale structures is discussed.

2.2 Real Time Structural Health Monitoring Methodologies

The SHM methods are defined as continuous monitoring of structures with permanently installed sensors for understanding the presence of flaws with real time data acquisition and pattern identification. The most common SHM methods include strain monitoring (e.g., [6, 7]), system identification using accelerometers (e.g., [8, 9]) and the acoustic emission method (e.g., [10, 11]). The sensors are strategically mounted on structures and the data is collected continuously, Figure 2.

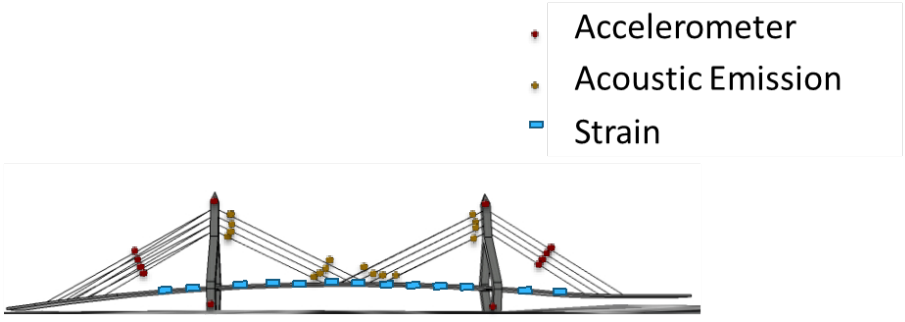

Figure 2: Distributed sensors on large scale structures for real time monitoring

Each method has advantages and disadvantages as shown in Table I. In this study, the challenges of the AE method are tackled by integrating efficient numerical formulations and

TABLE I: Comparison of three common SHM strategies for monitoring large scale structures

Method	Advantages	Drawbacks
Strain monitoring	Well-established method, Sensitive to static and dynamic strains	Influence of secondary sources such as temperature, Need of densely populated sensors for increasing sensitivity
System identification	Well-established method, Direct understanding structural properties such as vibrational modes and frequencies	Insensitive to small flaws, Need of densely populated sensors for extracting higher modes of vibration
Acoustic emission	Sensitive to micro-flaws, Capable of detecting and locating hidden defects, Global and local monitoring opportunity	Influence of background noise, Complex data collection process that challenges the repeatability and signal processing

multiphysics models. In the following section, a brief description of the AE method is presented.

2.3 Acoustic Emission (AE) Method

Acoustic Emission (AE) is a passive SHM method that relies on the propagating stress waves initiated by newly formed damage surfaces. The method requires loading the structure to the point where structurally insignificant micro-damage is intentionally created at the locations of existing damage, thereby releasing strain energy which initiates elastic waves which are then detected by surface mounted AE sensors. Therefore the AE method is used to detect a failure at a early stage of damage. This method is relatively inexpensive, since it only requires

a few sensors to be mounted at strategic locations to provide global health monitoring of a structure, including locations that are difficult to access by more localized techniques such as strain monitoring.

2.3.1 Quantitative AE Method

The AE method is a proven technology to evaluate the condition of civil infrastructures [12]. However, the mixture of damage signals and background noise signals is a challenge for implementing the AE method in various engineering applications. Source location/cluster-based analysis and frequency-based filtering are two typical techniques integrated with a multi-dimensional pattern recognition algorithm to differentiate extraneous noise and damage sources. The application of pencil lead break (PLB) on a test structure as described in ASTM E976-05 generates an impulse-like force-time function, simulating a discrete small crack growth. Practical AE testing makes use of the difference in the frequency spectrum of propagating elastic waves due to the PLB test and the frequency spectrum of the background noise. The approach has several limitations. The lead break is conducted on the surface and generates a mono-pole source while the actual damage may be beneath the surface and generates a bi-pole source. A better scientific understanding of the characteristics of elastic waves due to damage mechanisms in a structure is needed for developing a quantitative measurement approach of damage (e.g. frequency content, type, orientation) based on the AE method.

Acoustic emission sources are broadband in nature in the shape of a pulse-like function of stress [13]. The transfer function of the structure controls the frequencies and waveform signatures reaching the AE sensor, which depend on the material and geometry of the structure.

Finally, the AE sensor converts the surface motion into an electrical signal based on its transfer function. Using the transfer functions of the measurement components as shown in Figure 3, the recorded signal is obtained by the following formula [14]:

$$Rec\,(f) = S\,(f) * TF_G\,(f) * TF_S\,(f) * TF_R\,(f) \tag{2.1}$$

where Rec represents the recorded signal, S is the source function, TF_G is the transfer function of the material, TF_S represents the transfer function of the sensor and the coupling, and TF_R is the transfer function of the instrument.

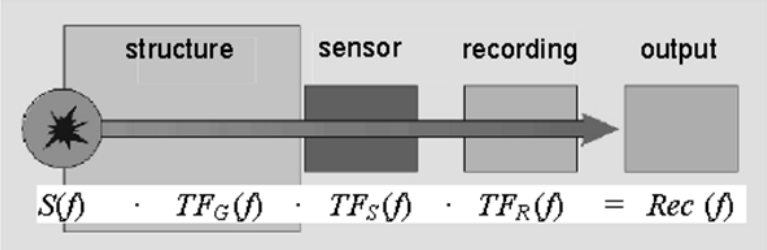

Figure 3: Concept for transfer functions

The process of obtaining the output signal indicates the complexity of the AE method. Typically, the AE waveforms are recorded, and then the AE features are extracted from the waveforms, which are implemented as descriptors of pattern recognition methods. For instance,

Figure 4 shows the AE features as risetime, duration, amplitude and energy of an AE signal. The quantitative AE method requires understanding all the variables that can influence the AE signal, and then recognizing the primary mechanisms (e.g., crack growth) and the secondary mechanisms (e.g., friction emission) in a given data set with real time pattern recognition methods.

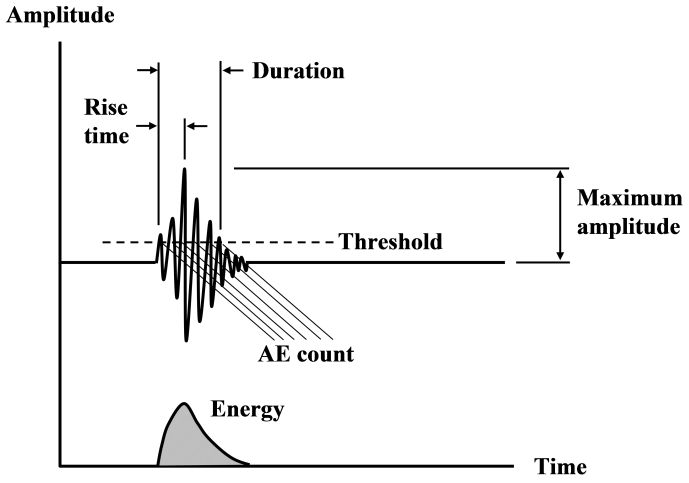

Figure 4: Common AE features extracted from AE signals

2.3.2 small-scale versus Large Scale Testing

As discussed above, pattern recognition methods are typically utilized in order to understand the damage state and types in a given AE data set. The proper implementation of pattern

recognition methods depends on the selected feature set resulting in the greatest separation among damage modes and secondary sources such as friction. Understanding the patterns due to different types of flaws can be achieved either through experimental designs or numerical models. The characteristics of a damage source depend on several variables such as volume of deformation, type, and orientation, and multiple sources that may be triggered simultaneously such as fiber breakage and matrix cracking in composites. The AE features implemented to find the patterns in relation to damage sources include time domain features such as amplitude, duration and energy as shown in Figure 4, and frequency domain features such as peak frequency and frequency centroid. As the characteristics of various damage sources are quite complex for the AE method, most pattern recognition approaches depend on experimental data using small-scale coupons. For instance, Sung et al. [15] monitored impact using neural networks while the distance between the structural boundary and the sensors was 30 mm, which means that the arrived elastic waves due to impact would sum with the reflected waves from the boundary; therefore, the impact source feature set would not be applicable to larger structures. Bhat et al. [16] developed artificial neural network schemes for composite failures using 280 mm x 35 mm specimens. There are many other examples in the literature related to pattern identifications using the AE data set from coupon specimens in composites [17–22] and metals [23, 24]. When the AE characteristics are based on the limited boundary coupon specimens, they are not directly applicable to large scale structures where boundary reflections are omitted from the selected time window of the recorded waveforms. There are limited examples of large scale testing of structures [10, 11] because of complexity and cost. A definite link between small-

scale and large scale experiments is needed for transferring the pattern recognition results to different scales. It is hypothesized that current knowledge of finite element modeling can tackle this problem with the development of effective formulations. In the following section, a general solution of the wave propagation problem is presented, and the methods proposed to solve the wave equation for large scale structures are discussed.

2.4 A General Solution of Homogeneous Wave Equation

The elastic wave equation for isotropic, heterogeneous material is

$$\mu\nabla^2\mathbf{u} + (\mu+\lambda)\,\nabla\nabla.\mathbf{u} - \rho\,\ddot{\mathbf{u}} = \mathbf{f} \tag{2.2}$$

where $\mathbf{u} : \Omega X(0,\tau] \rightarrow \mathbf{R}^2$ is the displacement and $\mathbf{f} : \Omega \rightarrow \mathbf{R}^2$ is the source, μ and λ are Lame constants and ρ is the density of the material. The weak formulation of the elastic wave equation is obtained by taking a dot product of Equation 2.2 with a vector weighting function integrated over the medium and appplying the divergence theorem

$$(\lambda+\mu)\int_\Omega (\nabla.\mathbf{u})\,(\nabla.\mathbf{v})\,d\Omega + \mu\int_\Omega (\nabla\mathbf{u} : \nabla\mathbf{v})d\Omega = \rho\frac{\partial^2\int_\Omega (\mathbf{u}.\mathbf{v})\,d\Omega}{\partial t^2} \tag{2.3}$$

$$\nabla u : \nabla v = \sum_{i=1}^{n}\sum_{j=1}^{n}(\nabla u)_{ij}(\nabla v)_{ij}$$

where $\mathbf{v}$ is the weighting function [25]. From the application of separation of variables and the Galerkin formulation, the following well known differential equation for forced vibration $\mathbf{F}$ is obtained:

$$\mathbf{M}\,\ddot{\mathbf{u}} + \mathbf{C}\,\dot{\mathbf{u}} + \mathbf{K}\mathbf{u} = \mathbf{F} \tag{2.4}$$

where $\mathbf{M}$, $\mathbf{K}$ and $\mathbf{C}$ are mass, stiffness and damping matrix respectively. The numerical modeling of wave propagation in complex structures increases the successful implementation of wave propagation and scatter-based SHM methods such as Ultrasonics and AE to detect the presence of damage and identify its impact on the remaining life of structures. For instance, the numerical solutions provide an efficient way for selecting the correct frequency range for Ultrasonic testing and a basis for pattern recognition approach for Acoustic Emission to detect and locate cracks in structures. Numerical methods such as the finite element method (FEM) and the finite difference method have been widely used to model elastic wave propagation [26, 27].

2.4.1 Challenges of Classical Finite Element Approach for the AE Method

The ability to accurately model elastic waves offers significant potential for differentiating noise from the signatures of damage and improving the interpretation of AE data [4]. In addition to understanding the frequency content of elastic waves due to damage mechanisms, the models can be used to identify the optimal sensor placement and the scaling of laboratory tests into large structures as in real life applications. The analytical solutions for wave propagation are limited to simple geometries [5]. Numerical methods (e.g. Finite Element) are needed to understand the wave propagation phenomena in complex geometries. The oscillatory nature of the wave equation requires fine meshing for a stable numerical approximation, which causes significant

computational complexity [28]. The frequency range of interest for typical AE applications is from 20 kHz up to 500 kHz. Suitable time interval Δt and element size l suggested for finite element calculations of propagating elastic waves for a stable solution without any numerical pollution [29] are

$$\Delta t = \frac{1}{20 f_{max}} \quad l = \frac{\lambda_{min}}{20} \tag{2.5}$$

where f_{max} is maximum frequency of interest and λ_{min} is the minimum wavelength involved. As an example, for 500 kHz as the maximum frequency of interest, a time interval of 0.1 μsec and element sizes of 0.5 mm for longitudinal waves (assuming cp=5000 m/sec) and 0.3 mm for shear waves (assuming cs=3000 m/sec) are required for a stable solution. Number of elements to model a 304.8 mm square plate with thickness of 25.4 mm is about 8 million. Considering the time interval as 0.1 μsec, modeling wave propagation requires significant processing power and time. Depending on the geometry, the model can be idealized as plane stress, plane strain, or axisymmetric to reduce the dimensions from 3D to 2D; however, that approach may not be functional if the geometry is complex and if the sensors are included into the model. Considering the size of civil infrastructures, modeling full scale geometry for wave propagation is not feasible. An effective FE design needs to be developed to reduce the number of elements to reach a stable and accurate solution.

2.4.2 Spectral Element Approach

Spectral elements are special forms of finite elements, which are based on the nodal coordinates of Lagrange shape functions obtained from the solutions of the orthogonal polynomials such as Legendre and Chebyshev. The mathematical formulation of finite elements using the

spectral elements allows modeling high frequency wave propagation more efficiently than standard FEM, which requires significantly fine meshing and small time steps to prevent dispersion pollution. Patera [30] demonstrated the effectiveness of the spectral element method (SEM) for fluid dynamics. There are two different kinds of spectral element methods, which have been used in literature addressing wave propagation analysis [30, 31]. The first approach is based on the frequency domain solution of the wave equation, which is accurate for only simple one-dimensional or two-dimensional problems. The second approach is based on the time domain solution of the wave equation using explicit or implicit methods, which can enhance high precision for analyzing wave propagation in complex geometries [32]. The spectral element method uses weighted residual techniques and high-order orthogonal interpolation functions [33]. The coordinates of the orthogonal polynomials such as Chebyshev or Legendre identify the nodal coordinates of the basis function. The spectral convergence rate is reported as faster than a power of $\frac{1}{n}$, when n is the order of selected orthogonal polynomial [34].

Spectral elements to solve multi-dimensional elastodynamic problems have been recently studied. For instance, Kudela [35] demonstrated the wave propagation modeling in 1D structures using Gauss-Lobatto-Legendre (GLL) points based on the 7th order Legendre polynomial. The GLL points result in a diagonal mass matrix, which enables the use of explicit methods to reduce the computational time of the dynamic wave equation solution. Zak [36] employed Chebyshev polynomials of the first kind to a 2D plate problem. Zak [37] also analyzed the wave propagation in rod structures and discussed the effects of some parameters, such as the selection of the orthogonal polynomial, on the accuracy of the numerical solution. Kudela [34] and

Kim [38] extended the problem to 3D including wafer type piezoelectric transmitters into the model for Lamb wave propagation analysis. To address the issues related to modeling wave propagation in complex geometries such as mesh distortion or locking effect, Witkowoski [39] studied the behavior of propagating waves through joints in the L-shape structures and concluded that the locking effect has not occcurred with high order spectral finite element formulation and that the accuracy of these formulations is not compromised by presence of distorted meshes. De Basabe [25] derived the stability condition and investigated the dispersive behavior of the spectral element method for acoustic and elastic wave equations. The authors showed that increasing the order of SEM reduces the dispersion error. To investigate the effect of damage in plate structures, Peng [40] applied three-dimensional spectral elements and demonstrated the efficiency of the method in Lamb wave propagation. Mehdizadeh [41] studied the efficiency of spectral elements for Helmholtz's equation. However, there is no study in the literature regarding which orthogonal polynomial order provides the optimized solution for elastic wave equations in terms of computational time and power for high frequencies. Kim [38] used the spectral element of polynomial order 5 with 10 nodes per wavelength and showed the efficiency of the spectral element for a particular polynomial order. While the convergence of the spectral element solution is reported as $\frac{1}{n}$, the computational time also increases with the increase in the polynomial order.

2.4.3 Effective Non-Reflective Boundary Conditions

Although the numerical solution of wave motion was initially formulated on an unbounded domain, the use of the domain discretization method necessitates truncating the domain by

setting artificial boundary conditions. The non-reflective boundary condition prevents any numerical reflections from boundaries back into the solution domain with a stable solution. In any absorbing boundary condition (ABC) approach, the Sommerfeld radiation condition [42] must be satisfied at the boundary for two orthogonal wave motions, P and S waves:

$$\lim_{R\to\infty} R^{\frac{d-1}{2}} \left(\frac{\partial u_p}{\partial R} - ik_p u_p \right) = 0 \tag{2.6}$$

$$\lim_{R\to\infty} R^{\frac{d-1}{2}} \left(\frac{\partial u_s}{\partial R} - ik_s u_s \right) = 0 \tag{2.7}$$

where R is the radial distance, d is the dimension of the problem, k_p and k_s are wave numbers for P waves and S waves, u_s and u_p are displacement fields for P waves and S waves.

There are two different approaches to truncate the computational domain without disturbing the solution of the original problem [43]. One of the methods is transparent boundary condition (TBC), which minimizes the reflection generated by the interface using differential operators. TBCs could be either local or non-local. Non-local types of TBCs are more accurate while computationally expensive compared to local types [44]. Absorbing boundary layers are other groups of methods that apply to simulate the infinite medium [45]. Absorbing boundary layers are finite-artificial layers which enclose on all sides of the computational domain in order to attenuate incoming waves [46].

In recent years, different formulations for absorbing layers have been proposed in the literature such as damping layers [47, 48], optimized conditions [49] and paraxial conditions [50]. One of the ideal absorbing layers is the Perfectly Matched Layer (PML), because it is local in

time and space, easy to implement and sufficiently accurate. The PML is an artificial layer, which provides an exponential decay regardless of frequency or angle of incidence and does not produce any reflection from the interface. Berenger [51] introduced the perfectly matched layer concept, and applied the PML to the Maxwell's equations for truncating wave propagation in a section of an unbounded domain. Although Berenger was successful in demonstrating the superiority of his methodology over some local boundary conditions [52], it has been shown that the split filed components equations used by Berenger are weakly ill-posed [53]. Chew [54] introduced complex coordinate stretching functions which map the spatial coordinates on to complex space. An unsplit-field finite difference PML formulation using the classical stretching function was suggested by Wang [55]. Basu and Chopra, in [56, 57] presented time-domain, displacement-based equations for elastodynamic medium and finite element (FE) algorithms for these equations, which are implemented in this study.

CHAPTER 3

SPECTRAL ELEMENT FORMULATION OF ELASTIC WAVE EQUATION

The content presented in this chapter was previously partially published in the proceeding of the SPIE 2013 conference of Smart Structures/NDE as "The selection of spectral element polynomial orders for high frequency numerical wave propagation" with my research advisor Dr. Ozevin as the co-author [1].

3.1 Introduction

In this section, the ideal polynomial order selection and the element size are identified for the most effective numerical model in terms of accuracy and computational time. The required polynomial order and the element size to obtain an accurate result for frequencies from 100 kHz to 400 kHz are discussed using L_2 norm analysis. The spectral element results are compared with conventional finite element models (FEM) using COMSOL Multiphysics software.

3.2 Governing Equations and Spectral Element Formulation

3.2.1 Nodal Coordinates and Basis Function

The discrete locations of the nodal coordinates are defined by the Gauss-Lobatto-Legendre (GLL) points using the selected Legendre polynomial degree, which defines the p refinement within the element. The GLL points are calculated by the roots of following equation [35]:

$$\left(1-\xi^2\right)\frac{dP_N(\xi)}{d\xi}=0 \tag{3.1}$$

where $dP_N(\xi)$ is the Legendre polynomial of degree N and $\xi \in [-1,1]$. The basis function $h_i = (0, ..., \text{number of node})$ using the Lagrange interpolation polynomials [33]:

$$N_{ij}=\prod_{m=0,m\neq i}^{n}\frac{(\xi-\overline{\xi}_m)}{(\overline{\xi}_i-\overline{\xi}_m)}\prod_{l=0,l\neq j}^{n}\frac{(\eta-\overline{\eta}_l)}{(\overline{\eta}_j-\overline{\eta}_l)} \tag{3.2}$$

where ξ and η are the natural coordinate systems in the element and $\overline{\xi}_i$ and $\overline{\eta}_j$ are the coordinates of the ith and jth node in the direction of ξ and η, respectively. In this study, the Legendre polynomial orders of 3 to 5 are studied in addition to h refinement in order to find the computationally optimal spectral element modeling of different frequencies. Figure 5 shows the Lagrangian shape function using GLL integration points for the coordinate of (0.87, 0.87) for (ξ, η). The non-uniform distribution of nodal points reduces the presence of the Runge phenomenon [58].

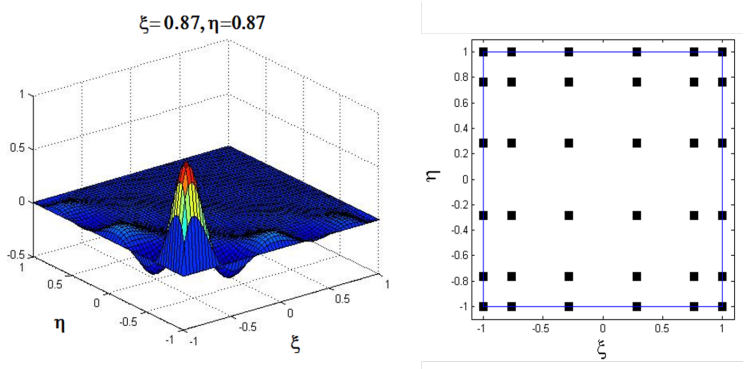

Figure 5: (a) The shape of Lagrangian 2D shape function for (0.87, 0.87) in natural coordinate system; (b) the GLL integration points on an element using Legendre polynomial degree of five

3.2.2 Finite Element Formulation

The elastic wave equation for isotropic, homogenous material is discussed in Chapter 2. The weak formulation of the elastic wave equation and the differential equation for the forced vibration **F** are shown in Equation 2.3 and Equation 2.4. The mass matrix **M** and the element stiffness matrix **K** are obtained using the shape functions in the natural coordinate system (ξ, η) as [59]:

$$\begin{aligned} \mathbf{M} &= \int_{-1}^{1}\int \rho \mathbf{H}^{\intercal}\mathbf{H} \det \mathbf{J} d\xi d\eta, \\ \mathbf{K} &= \int_{-1}^{1}\int \mathbf{B}^{\intercal}\mathbf{C}\mathbf{B} \det \mathbf{J} d\xi d\eta \end{aligned} \tag{3.3}$$

where **H** is a matrix of shape functions, **B** is the strain-displacement transformation matrix, **C** is the material stiffness matrix, **C** is the Jacobian operator. The 2D plane stress problem

for an isotropic material (steel) was formulated using the Legendre polynomial. The kinematic equations are:

$$\begin{bmatrix} \varepsilon_x \\ \varepsilon_y \\ \varepsilon_{xy} \end{bmatrix} = \begin{bmatrix} \frac{\partial u}{\partial x} \\ \frac{\partial v}{\partial y} \\ \frac{\partial u}{\partial y} + \frac{\partial v}{\partial x} \end{bmatrix} \tag{3.4}$$

The same degree of Legendre polynomial is used in ξ and η directions associated with a shape function as discussed in the previous section. The shape function matrix and the strain-displacement transformation matrix are:

$$\mathbf{H} = \begin{bmatrix} h_1 & 0 & h_2 & 0 & \dots & h_m & 0 \\ 0 & h_1 & 0 & h_2 & \dots & 0 & h_m \end{bmatrix}_{2m} \tag{3.5}$$

$$\mathbf{B} = \begin{bmatrix} a\frac{\partial h_1}{\partial \xi} & 0 & a\frac{\partial h_2}{\partial \xi} & 0 & \dots \\ 0 & b\frac{\partial h_1}{\partial \eta} & 0 & b\frac{\partial h_2}{\partial \eta} & \dots \\ b\frac{\partial h_1}{\partial \eta} & a\frac{\partial h_1}{\partial \xi} & b\frac{\partial h_2}{\partial \eta} & a\frac{\partial h_2}{\partial \xi} & \dots \end{bmatrix}_{3m} \tag{3.6}$$

where m is $(number\ of\ node)^2$ and a and b are directly related to Jacobian. The constitutive matrix $\mathbf{C}$ for plane stress is :

$$\mathbf{C} = \frac{E}{(1-\nu^2)} \begin{bmatrix} 1 & \nu & 0 \\ \nu & 1 & 0 \\ 0 & 0 & \frac{1-\nu}{2} \end{bmatrix} \tag{3.7}$$

Using equations Equation 2.4 and Equation 3.3 the wave propagation problem for three-cycle sinusoidal loading with varying frequencies was solved and compared with COMSOL Multiphysics in terms of accuracy and computational time efficiency. The numerical solutions of the mass and stiffness matrices were found using the GLL (Gauss-Lobatto-Legendre) integration:

$$\begin{aligned} K_{ij} &= \sum_{m=1}^{n} w_m \sum_{l=1}^{n} w_l k_{ij}\left(\xi_m, \xi_{\xi l}\right), \\ M_{ij=} &\sum_{m=1}^{n} w_m \sum_{l=1}^{n} w_l m_{ij}\left(\xi_m, \xi_{\xi l}\right) \end{aligned} \tag{3.8}$$

where $w_m = \frac{2}{n(n-1)[p_{n-1}(\xi_m)]^2}$. The dynamic equation was solved using the implicit special case of Newmark's method called average acceleration, which is unconditionally stable.

3.2.3 Structural Geometry and Boundary Conditions

The spectral element is modeled on a steel plate with the dimensions as thickness 1 *mm*, width 100 *mm* and height 50 *mm*. The plate is divided into square elements as shown in Figure 6 indicating the nodal coordinates of the third order Legendre polynomial. The material properties are taken as 200 *GPa* for Young's Modulus, 7850 $(kg)\,(m)^{-3}$ for density and 0.33 for Poisson's ratio. The geometry is idealized as a plane stress problem due to the model thickness. A three-cycle sinusoidal load with unit amplitude is applied at the edge of the plate. The frequency of the dynamic load is varied as 100 *kHz*, 200 *kHz*, 300 *kHz* and 400 *kHz*. The other end of the plate is modeled as the fixed boundary. The displacement histories of the spectral element result and conventional FE result are compared at the top-middle point of the plate.

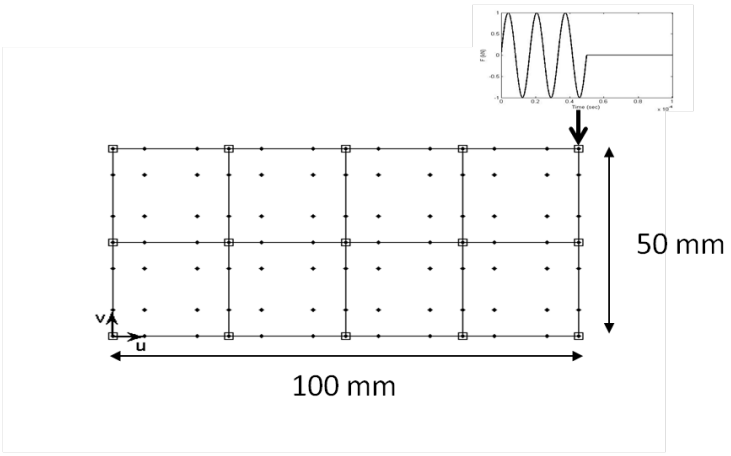

Figure 6: Geometric configuration

3.3 The Accuracy of Spectral Element Formulation

The numerical simulations of frequencies in the range of 100 *kHz* to 400 *kHz* are repeated using the conventional finite element formulation. The geometry is meshed with the resolution of $^1/_{20^{th}}$ of wavelength using the wave velocity as 5000 $(m)\,(sec)^{-1}$ in COMSOL Multiphysics software with the same material properties and boundary conditions. The displacement histories in the -y direction at 50 *mm* away from the loading point are compared. The solution of the conventional FE formulation is considered as the correct wave histories for comparison with the spectral element formulation. For each polynomial order, the element size is gradually decreased until the spectral element solution matches the conventional finite element solution. As an example of the spectral element converging to the finite element result, Figure 7 shows the results of polynomial order 4 for 400 *kHz* excitation with a decrease in element size to

reach to the same displacement history as the finite element result. The spurious waves and the incorrect wave velocities are clearly seen in Figure 7(a) when the nodal resolution is insufficient to prevent dispersion pollution. The wave amplitude is also incorrectly calculated when the spatial resolution is insufficient. Figure 7(d) shows the acceptable match of two numerical solutions. Similar convergence studies are performed for other frequencies by changing the polynomial order and element size in order to find the optimal spectral element in terms of accuracy and computational time. Note that the step size for time integration is the same for both SEM and FEM models.

3.4 The Selection of Polynomial Order and Element Size

The polynomial orders of 3 to 5 are studied with varying element size for all the frequencies, and the displacement histories are compared with the finite element results. The comparison is conducted through the L_2 norm analysis $\|e_2\|$ defined as [41]:

$$\|e_2\| := \sqrt{\sum (u_{spectral\ element} - u_{classical\ finite\ element})^2} \tag{3.9}$$

Figure 8 shows the convergence of the spectral element solution depending on the decrease in the element size and the polynomial order. For the same size element, the error is the smallest for the higher-order polynomial except for the 400 *kHz* excitation. The convergence rate is different depending on the target frequency and the polynomial order. For instance, for the 100 *kHz* excitation, the error using 3^{rd} order polynomial is higher than 5^{th} order polynomial for

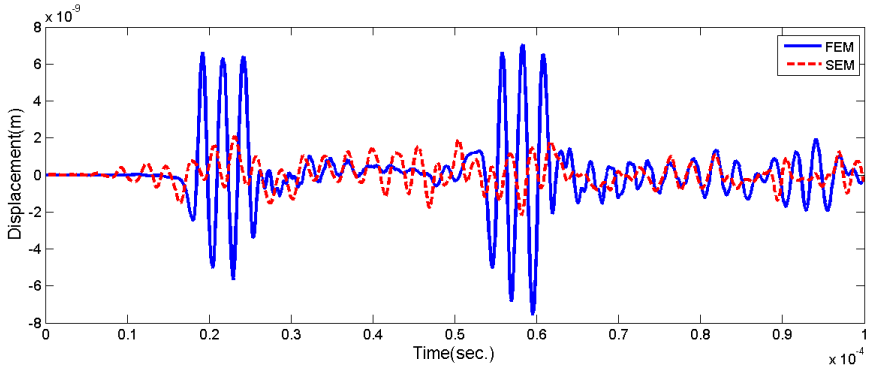

(a) $16.7mm$

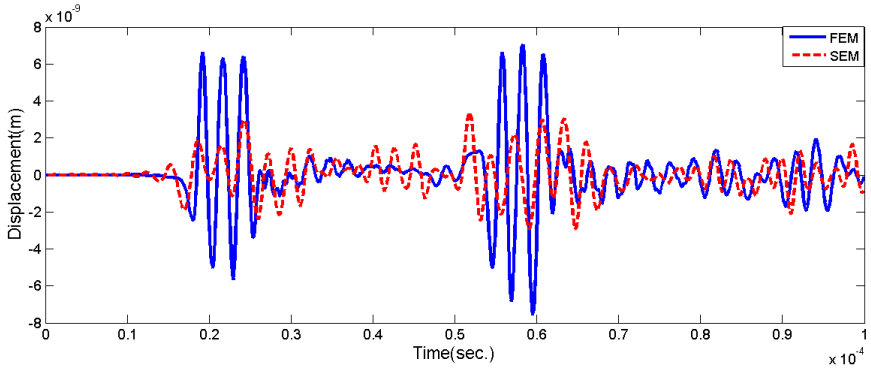

(b) $10mm$

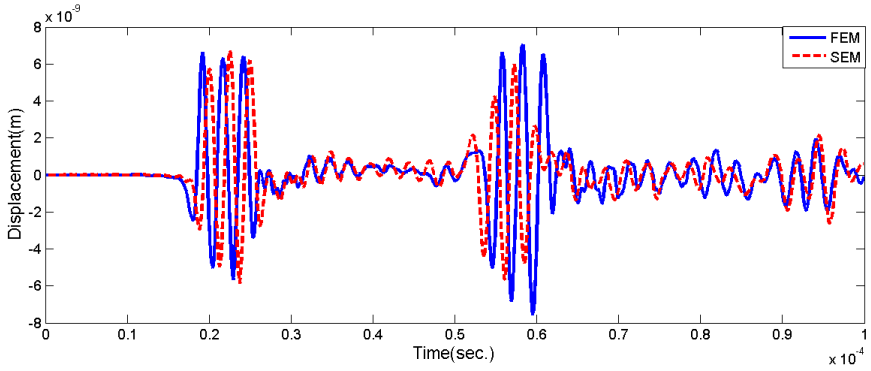

(c) $5mm$

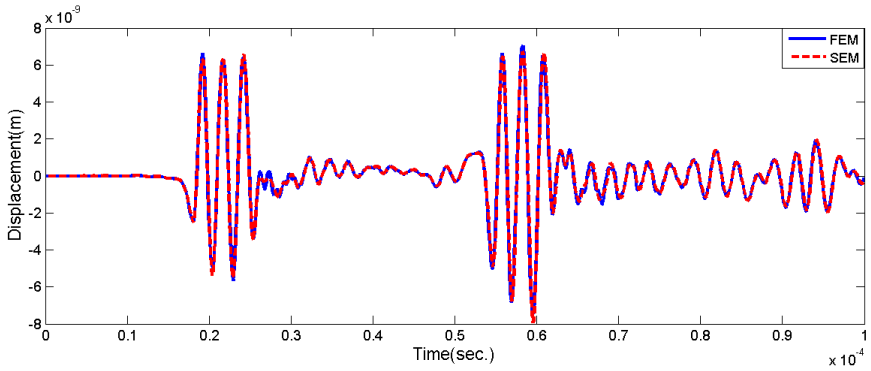

(d) $3.3mm$

Figure 7: Decreasing dispersion with h-refinement in spectral element for the 4^{th} order polynomial and 400 kHz excitation

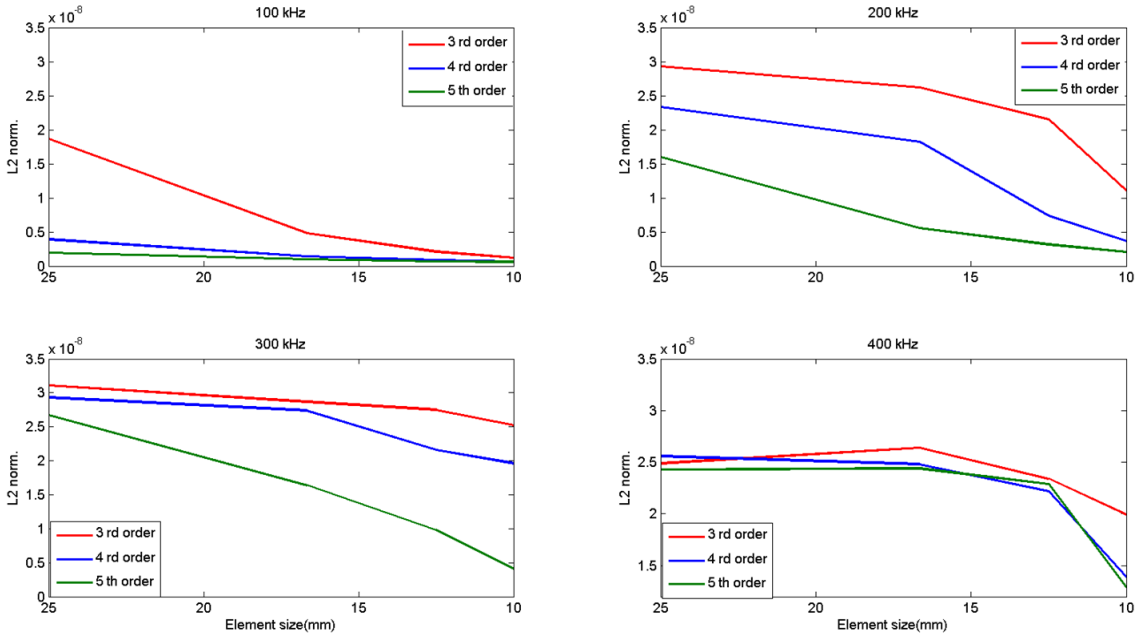

Figure 8: L_2 norm results for 400 kHz, 300 kHz, 200 kHz, 100 kHz and different polynomial orders as 3,4,5

the largest element size. However, for the 400 *kHz* excitation, the errors for all the polynomial orders are similar. The increase in the required frequency resolution causes similar convergence rates for different polynomial orders.

In order to reach the error norm less than 2×10^{-11}, the element size is gradually decreased to reach a good match with FEM as shown in Figure 9 for the fourth order polynomial. The first wave arrivals and the reflected wave arrivals perfectly match for the frequencies from 100 *kHz* to 400 *kHz*. There is no damping introduced into both models. The arrivals of wave envelope with three cycles are seen clearly for higher frequencies. Because of a higher period of 100 *kHz*, the

TABLE II: The required spectral element formulation per frequency and computational time for polynomial orders as (3,4,5)

Frequency (kHz)	Element size (mm)	L_2 norm$\times 10^{-11}$	Number of nodes per wave-length	Computational Time(spatial Integration)(sec.)	Computational Time(Time Integration)(sec)
100	(10,12.5,16.6)	(12.2,8.80,9.87)	(18,17,15)	(15.8, 34.3, 120.8)	(1.62, 7.0, 5.50)
200	(5,6.25,10)	(18.2,9.97,15.6)	(18,16,17)	(30.1, 50.4, 122.2)	(415, 647, 165)
300	(3.8,5,6.25)	(18.3,15.8,16.4)	(17,16,17)	(100.3, 95.8, 162.4)	(2.6,3.02, 3.02)x10^3
400	(2.7,3.3,5)	(18.1,17.3,16.2)	(17,18,15)	(573.3, 666, 270.1)	(2.2,4.11, 2.25)x10^4

first wave arrival is combined with the reflected wave from the boundary. The required spectral element sizes for each frequency and polynomial order to reach to the target error norm are provided in Table II. The element size decreases when the polynomial order increases as there are more computational points within each element. The table also summarizes the required node number per wavelength using the wave velocity in steel as 5710 $(m)\,(sec)^{-1}$ [5]. The range of node number per wavelength is 15-18 which can be used a guide for selecting the element size and the polynomial order.

The other factor for selecting the element size and polynomial order is the computational time. The computational time of the spectral element calculation is divided into two parts: spatial integration to calculate mass and stiffness matrices and time integration. It is important to note that the spectral element formulation is conducted using the Matlab program;

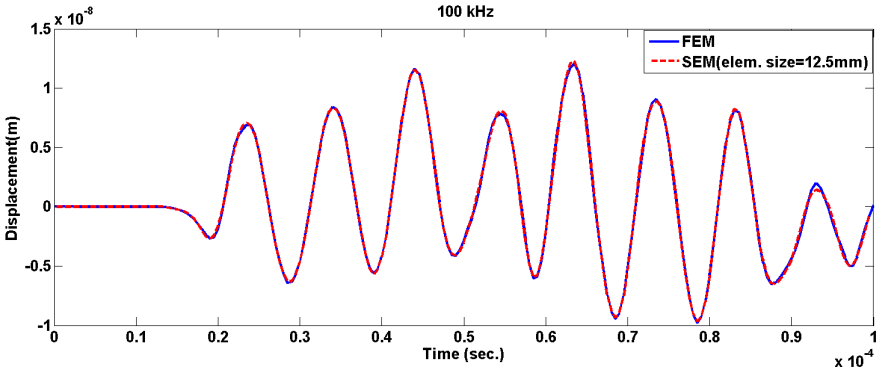

(a) $100kHz$

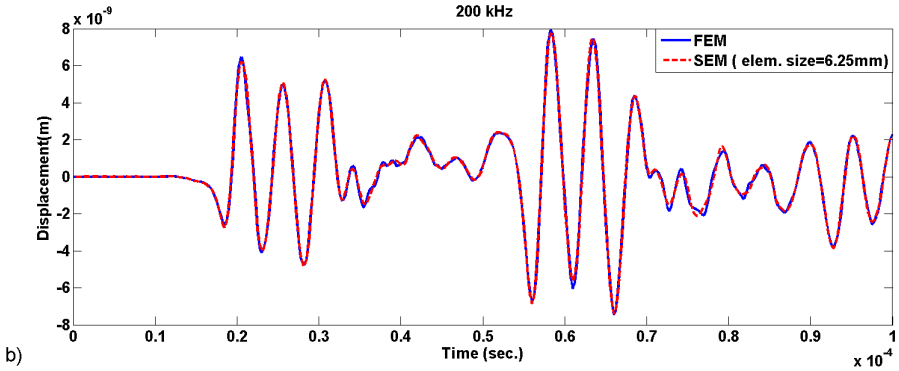

b)

(b) $200kHz$

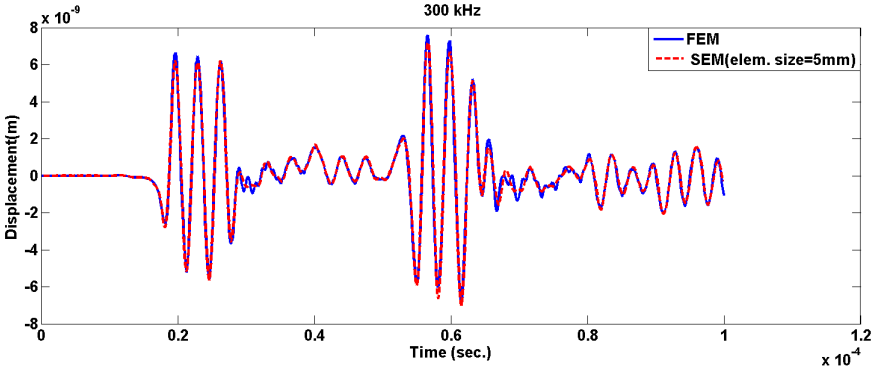

c)

ze

(c) $300kHz$

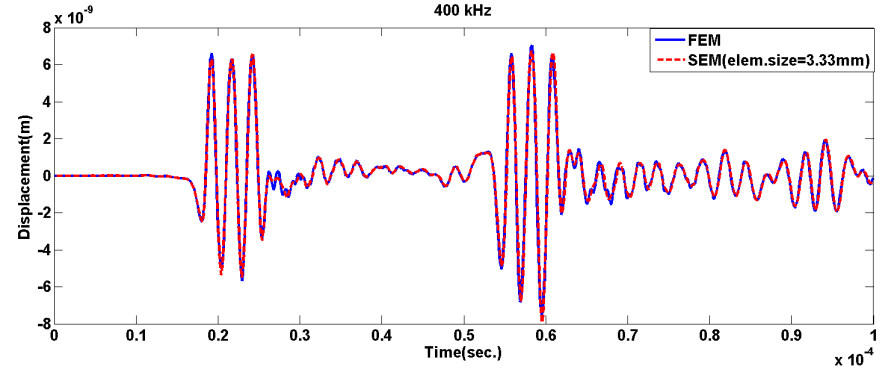

d)

(d) $400kHz$

Figure 9: Comparison between COMSOL and spectral element

the algorithm calculation can be improved further with better programming and a different programming language. Table II shows the computational times for numerical integration and time integration separately. When the frequency resolution is increased, there is a dramatic increase in numerical computations of stiffness and mass matrices with the increase in the polynomial order as indicated. For instance, for the 400 *kHz* resolution, the computational times for the numerical integration using the third, fourth and fifth order polynomials are 573.3, 666 and 270.1 *sec*, respectively. The numerical integration time of stiffness and mass matrices for each element depends on the polynomial order. Unless high frequency resolution is needed, the polynomial orders 3 and 4 are computationally more efficient than the polynomial order 5.

3.5 The Efficiency Comparison of SEM and FEM

Table III shows degrees of freedom for four different frequencies required for FEM and SEM formulated using the fourth order polynomial. It is clearly advantageous to use the spectral element method for higher frequencies. As the required frequency resolution increases, the difference between degrees of freedom increases dramatically. For instance, the degrees of freedom difference between two methods approximately doubles when the frequency resolution is increased from 300 *kHz* to 400 *kHz*. In addition to the reduction in the degrees of freedom of SEM, the diagonal mass matrix increases the computational efficiency in time integration. While reducing the time step does not have significant influence on the computational time of the spectral element because of diagonal mass matrix property, the computational time increases significantly for the classical finite element formulation. For example, for the 100 *kHz* frequency resolution, the computational time of FEM increases four times when the time step

reduced from 0.5 μs to .25 μs, while the computational time remains almost the same for SEM.

TABLE III: Number of degree of freedom for each method for different frequencies

Frequency (kHz)	Element Size (mm)		Number of Degree of Freedom		Difference
	FEM	SEM(4th order)	FEM	SEM	
100	2	12.5	13842	1088	12754
200	1.25	6.25	54882	4224	50658
300	0.8	5	135704	6560	129144
400	0.6	3.33	240914	14640	226274

3.6 Summary

In this chapter, a detailed investigation of spectral element formulation for different Legendre polynomial orders and frequency resolution is performed for the elastodynamic problem of an isotropic plate. The node per wavelength value can be used for identifying the polynomial order and the element size. Erroneous waveforms due to insufficient node per wavelength ratio have been demonstrated with incorrect wave velocity, wave amplitude and spurious wave motions. The critical element sizes for different polynomial orders are identified. The followings are the main results of this chapter:

- The required degrees of freedom to solve high frequency wave equation dramatically decrease with the SEM formulation.

- When the polynomial order increases, the computational times of numerical integration of mass and stiffness matrices increase significantly as the size of element matrix becomes higher. For instance for 400 kHz frequency, the computation times of numerical integration for the fifth order polynomial is increased almost five times compared to the fourth order polynomial.
- When the size of the structural geometry increases, higher-order polynomials require larger element size, which may be more efficient to use in terms of computational time and accuracy.
- As a general approach, the node per wavelength as average 16 provides the accuracy to formulate the spectral finite element model of elastodynamic problem, which can be used for the identification of element size after the polynomial order is selected.

It is clearly shown that the advantage of spectral element formulation increases with the increase of the frequency. The selections of the element size and the polynomial order depend on the required frequency resolution. The results presented herein are based on plane stress condition and square element use.

CHAPTER 4

CASE STUDY: WAVE PROPAGATION IN LONG-RANGE PIPE STRUCTURES

The content of this chapter was previously published as "Efficient computation of wave propagation along axisymmetric pipes under non-axisymmetric loading" in the journal of "Finite Elements in Analysis and Design" with my research advisor, Dr. Ozevin, as the co-author [3].

4.1 Introduction

This chapter presents an application of the spectral element formulation to study wave propagation in long-range pipelines. An efficient formulation of the problem of wave propagation along the length of axisymmetric pipes under non-axisymmetric loading such as leaks or new cracks is developed such that wave characteristics in a long-range pipe can be identified without the excessive computational time associated with the most current 3D modeling techniques. The axisymmetric geometry of the pipe is simplified by reducing the problem to 2D while the non-axisymmetric loading is represented by the summation of Fourier series. Since the pipe stiffness matrix as conventionally formulated represents the greatest single computational load, the strain-displacement matrix is partitioned in such a way that numerical integration components are decoupled from θ (the angular parameter) and n (the number of Fourier terms). A single numerical integration of the strain-displacement matrix is performed and utilized for

all the iterations of Fourier terms to represent the non-axisymmetric load. The computational efficiency of the developed method is compared with conventional finite element tools.

4.1.1 Elastic Wave Propagation in Pipe

The main wave propagation based SHM methods for pipelines are guided wave ultrasonics and acoustic emission. Guided wave ultrasonics relies on capturing the reflected wave energy from a defect after introducing a perturbation signal using ultrasonic transducers [60, 61]. If less-dispersive guided modes are selected to transmit and receive the signal, long-range pipes can be monitored using a limited set of transducers. The acoustic emission (AE) method relies on propagating elastic waves emitted from newly formed damage surfaces such as active cracks and leaks. Crack growth causes sudden stress-strain change in its vicinity, which generates a wideband step function. A leak causes turbulence at its location, which generates continuous emissions. The AE method may be based on elastic waves propagating through the pipe material [62, 63] or acoustic waves propagating through the material inside the pipe [64]. For an effective and accurate monitoring approach, wave characteristics such as the dispersion curves under buried or fluid filled conditions and the attenuation profile should be known prior to the implementation of an SHM method. However, experimental simulations of different pipe geometries and conditions are generally not possible. Wave propagation in pipes is a complex phenomenon due to the excitation of multi-mode waves, which must be superimposed to provide an overall solution. Analytical solutions of governing differential equations are not applicable when the pipe geometry becomes complex with the presence of defects, coatings and internal materials [65,66], buried conditions [67], and pipe bends [68]. The modeling of wave propagation

is important for quantitative understanding of damage mechanics and the identification of the SHM system characteristics (e.g. frequency selection, sensor position [69]). Wave propagation in pipes can be numerically modeled as 2D or 3D [70]. The 3D wave propagation problems of hollow circular cylinders including non-axisymmetric wave modes are formulated by Gazis [71]. If the problem requires modeling high frequency waves in a large scale structure, the 3D model becomes computationally expensive. Therefore, it is imperative to reduce the mathematical problem to 2D or implement a semi-analytical finite element formulation [72, 73] for reducing the computational load. When the structure and loading are axisymmetric, the structural model can be reduced to a 2D problem as displacements and stresses are independent of θ (the angular parameter). There are several other methods for reducing the computational time of high frequency wave propagation in hollow structures. Zhou et al. [74] applied the numerical eigenmode extraction method applicable to wave propagation in periodic structures. Mazzotti et al. [75] applied a Semi Analytical Finite Element (SAFE) method to study the influence of prestressing load on the dispersion of viscoelastic pressurized pipe. Bai et al. [73] constructed an elastodynamic steady-state Green's function based on modal data determined from the spectral decomposition of a circular laminated piezoelectric cylinder using a semi-analytical finite element formulation. Zhuang et al. [72] proposed integral transform and forced vibration as two different methods both based on the same set of eigenvalue data, to construct a steady-state Green's function for a laminated circular cylinder. Gsell et al. [76] discretized the displacement equations directly using the finite difference method, which reduced the computational time by 25%. When the structure is axisymmetric and the load is non-axisymmetric, three displacement

components in the radial, axial and circumferential directions exist [77, 78]. To utilize the 2D axisymmetric geometry of the pipe, the non-axisymmetric load can be expanded using Fourier series, and the structural response can be computed by superposing the solutions of each Fourier term [79, 80]. There are several examples in the literature related to applying Fourier series summation to model axisymmetric geometries with non-axisymmetric loading such as Zhuang et al. [72], Bai et al. [73], Wunderlich et al. [81] and Bouzid et al. [82]. However, in the case where the Fourier expansion of the load function requires many harmonics to represent the non-axisymmetric loads such as concentrated loads, the 2D superposition method combined with conventional finite element formulation may not be more computationally efficient than 3D analyses [59, 83]. Bathe [59] describes that the stiffness matrices corresponding to the different harmonics can be decoupled due to the orthogonal properties of trigonometric functions. However, to the best of our knowledge, there is no study that explicitly presents the mathematical formulation. While numerical models are capable of simulating various pipe geometries and conditions to deduce the waveform characteristics, existing numerical formulations for wave propagation are computationally expensive, and not practical for modeling long-range pipes.

4.2 Method of Analysis

The formulation is based on partitioning the strain-displacement matrix in such a way that the numerical integration terms are decoupled from the variables θ and n (the number of Fourier terms). Therefore, the strain-displacement matrix is calculated only once and used for each Fourier term calculation.

4.2.1 Coordinate System and Corresponding Displacement Fields

The cylindrical coordinates and the axis of revolution for pipe geometry are shown in Figure 10(a). The axial, radial and circumferential displacements are defined as w, u and v, respectively. The spectral element discretization of a cross sectional element using the 5^{th} order Legendre polynomial is shown in Figure 10(b). The axis of revolution is z with the displacement component w. In general, when loading has no symmetry and is defined by Fourier series components, the displacement components at radial (u), axial (w) and circumferential (v) directions can be defined in the form of Fourier expansion as [83]:

$$u = \sum_{n=1} (\overline{u}_n \cos n\theta + \overline{\overline{u}}_n \sin n\theta) \tag{4.1}$$

$$v = \sum_{n=1} (\overline{v}_n \sin n\theta - \overline{\overline{v}}_n \cos n\theta) \tag{4.2}$$

$$w = \sum_{n=1} (\overline{w}_n \cos n\theta + \overline{\overline{w}}_n \sin n\theta) \tag{4.3}$$

where n is the harmonic number. Single and double barred terms represent the symmetric and antisymmetric displacement amplitudes with respect to the plane $\theta = 0$ [83].

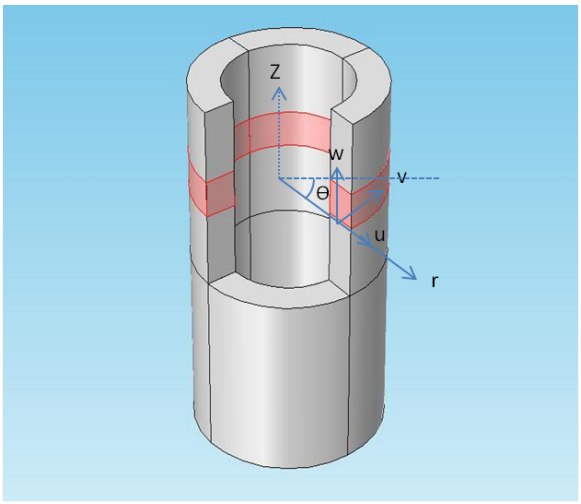

(a)

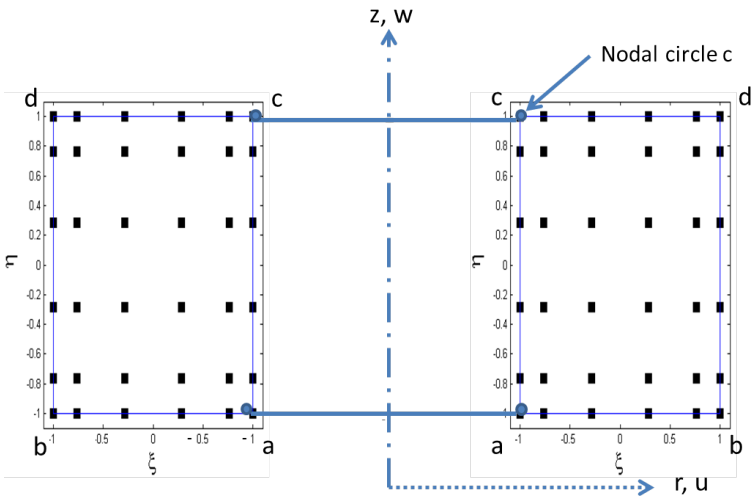

(b)

Figure 10: (a) Coordinates and displacement components of a pipe model, (b) spectral element discretization of an element

If the applied load is symmetric about the plane $\theta = 0$ and $n = 1, 2, 3, ...$, the terms of the single- barred series represent the displacement amplitudes, and double-barred components vanish. The double-barred terms are associated with additional antisymmetric loads. For instance, the $n = 0$ terms of the double-barred series are used to represent a pure torque [83]. However, for an isotropic elastic material, symmetric and antisymmetric terms are completely uncoupled and can be handled separately. In the case of antisymmetric harmonics, the stiffness matrix is identical to the symmetric case, which explains the appearance of negative sign in Equation 4.2. Therefore, all the formulations are almost the same as symmetric case [77, 83]. For the case of point loading at the circumference of the pipe, shown in Figure 11, loading becomes symmetric about the $\theta = 0$ axis, and the displacement components are simplified as:

$$\left\{ \begin{array}{c} u \\ v \\ w \end{array} \right\} = \sum_{n} \left\{ \begin{array}{c} \overline{u}_n \cos n\theta \\ \overline{v}_n \sin n\theta \\ \overline{w}_n \cos n\theta \end{array} \right\} \tag{4.4}$$

The concentrated load can be represented by various forms of Fourier series (e.g. [72, 84–86]). The Fourier series of the time dependent point load is defined as $P_N(\theta, t) = \delta_N(\theta) F(t)$ at $r = r_0$ and $z = z_0$. The delta function $\delta_N(\theta)$ and the load function (3-cycle sine wave) $F(t)$ are defined as:

$$\delta_N(\theta) = \frac{1}{2\pi} \frac{\sin\left(N + \frac{1}{2}\right)\theta}{\sin\left(\frac{1}{2}\theta\right)} \tag{4.5}$$

$$F(t) = \begin{cases} 10\sin(2\pi f t), & \text{if } t \leqslant \frac{3}{f} \\ 0, & \text{if } t > \frac{3}{f} \end{cases} \tag{4.6}$$

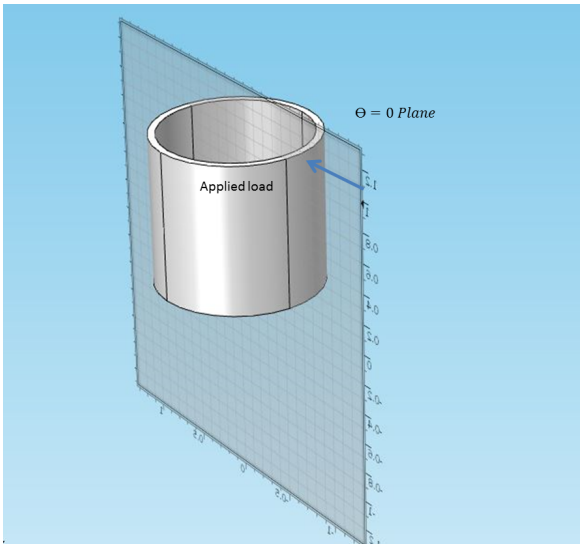

(a)

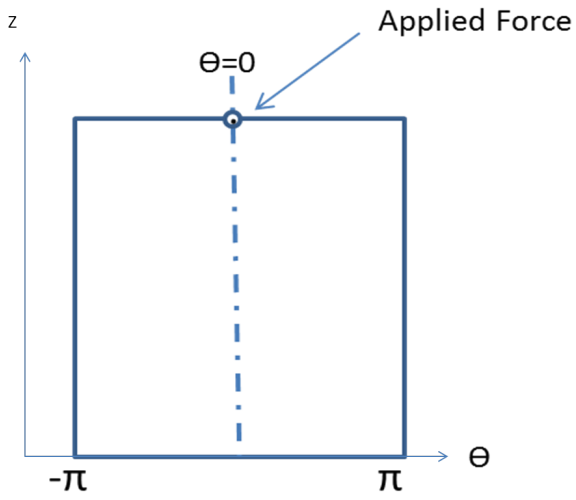

(b)

Figure 11: The symmetry of the point load for $\theta = 0$, (a) on a 3D view, (b) on a 2D view extending from -π to π

4.2.2 The Strain-Displacement Matrix

The approximation of the displacement fields for a 36-node element shown in Figure 10 can be written as:

$$\begin{Bmatrix} \overline{u_n} \\ \overline{v_n} \\ \overline{w_n} \end{Bmatrix} = \left[\begin{array}{ccc|ccc|c|ccc} N_1 & 0 & 0 & N_2 & 0 & 0 & ... & N_{36} & 0 & 0 \\ 0 & N_1 & 0 & 0 & N_2 & 0 & ... & 0 & N_{36} & 0 \\ 0 & 0 & N_1 & 0 & 0 & N_2 & ... & 0 & 0 & N_{36} \end{array}\right] \times$$

$$\left[\begin{array}{ccc|ccc|c|ccc} \bar{u}_{1n} & \bar{v}_{1n} & \bar{w}_{1n} & \bar{u}_{2n} & \bar{v}_{2n} & \bar{w}_{2n} & ... & \bar{u}_{36n} & \bar{v}_{36n} & \bar{w}_{36n} \end{array}\right]^T \tag{4.7}$$

Basis functions N_i are defined in Equation 3.2. The element displacements are written in the form as:

$$\begin{Bmatrix} u \\ v \\ w \end{Bmatrix} = \sum_n \begin{Bmatrix} \bar{u}_n \cos n\theta \\ \bar{v}_n \sin n\theta \\ \bar{w}_n \cos n\theta \end{Bmatrix} = \sum_n \begin{bmatrix} N_1 \cos n\theta & 0 & 0 & ... \\ 0 & N_1 \sin n\theta & 0 & ... \\ 0 & 0 & N_1 \cos n\theta & ... \end{bmatrix} \left\{\bar{d}\right\}_n \tag{4.8}$$

where $\{\bar{d}\}_n = \left[\begin{array}{ccc|ccc|c} \bar{u}_{1n} & \bar{v}_{1n} & \bar{w}_{1n} & \bar{u}_{2n} & \bar{v}_{2n} & \bar{w}_{2n} & ... \end{array}\right]^T$. The three-dimensional expression of strains in cylindrical coordinates is given by [81]:

$$\boldsymbol{\varepsilon} = \left\{\begin{array}{c} \varepsilon_r \\ \varepsilon_\theta \\ \varepsilon_z \\ \gamma_{rz} \\ \gamma_{r\theta} \\ \gamma_{z\theta} \end{array}\right\} = \left\{\begin{array}{c} u_{,r} \\ [u + v_{,\theta}]/r \\ w_{,z} \\ u_{,z} + w_{,r} \\ \frac{u_{,\theta}}{r} + v_{,\mathrm{r}} - v/r \\ u_{,z} + w_{,\theta}/r \end{array}\right\} \tag{4.9}$$

By substituting Equation 4.8 into Equation 4.9 and applying the operator matrix $[\partial]$,

$$\boldsymbol{\varepsilon} = [\partial] \left[\begin{array}{cccc} N_{n=1} & N_{n=2} & N_{n=3} & ... \end{array}\right] \{\bar{d}\} \tag{4.10}$$

$$\text{where } [\partial] = \left[\begin{array}{ccc|c} \partial/\partial r & 0 & 0 & ... \\ 1/r & \partial/r\,(\partial\theta) & 0 & ... \\ 0 & 0 & \partial/\partial z & ... \\ \partial/\partial z & 0 & \partial/\partial r & ... \\ 1/\left(r\partial\theta\right) & \partial/\partial r - 1/r & 0 & ... \\ 0 & \partial/\partial z & \partial/r\,(\partial\theta) & ... \end{array}\right].$$

The contribution of n^{th} harmonic to strain can be written as:

$$\{\varepsilon\}_n = [B]_n \{\bar{d}\}_n \tag{4.11}$$

where

$$\left\{\begin{array}{c} \varepsilon_{rn} \\ \varepsilon_{\theta n} \\ \varepsilon_{zn} \\ \gamma_{rzn} \\ \gamma_{r\theta n} \\ \gamma_{z\theta n} \end{array}\right\} = \left[\begin{array}{cccc} N_{1,r}\cos n\theta & 0 & 0 & ... \\ \left(N_1/_r\right)\cos n\theta & \left(nN_1/_r\right)\cos n\theta & 0 & ... \\ 0 & 0 & N_{1,z}\cos n\theta & ... \\ N_{1,z}\cos n\theta & 0 & N_{1,r}\cos n\theta & ... \\ -\left(nN_1/_r\right)\sin n\theta & (N_{1,r} - \left(N_1/_r\right))\sin n\theta & 0 & ... \\ 0 & N_{1,z}\sin n\theta & -\left(nN_1/_r\right)\sin n\theta & ... \end{array}\right] \times$$

$$\left[\begin{array}{ccc|ccc|c} \bar{u}_{1n} & \bar{v}_{1n} & \bar{w}_{1n} & \bar{u}_{2n} & \bar{v}_{2n} & \bar{w}_{2n} & ... \end{array}\right]^T \tag{4.12}$$

Equation 4.12 indicates that the strain-displacement matrix **B** depends on r, z, θ and n.

4.2.3 Decoupling the Stiffness Matrix

In order to calculate the structural response, one may compute the stiffness matrix for each Fourier harmonic of loading as **B** is functions of n and θ, and possibly different for each component of the total load. Therefore, superposition method becomes computationally expensive particularly in the case of a concentrated load, which requires many harmonics. To decouple the matrix from n and θ, **B** matrix is partitioned into two blocks:

$$\mathbf{B} = \left[\frac{A_1}{A_2}\right] \tag{4.13}$$

where

$$\mathbf{A_1} = \begin{bmatrix} N_{1,r}\cos n\theta & 0 & 0 & ... \\ \left(N_1/_r\right)\cos n\theta & \left(nN_1/_r\right)\cos n\theta & 0 & ... \\ 0 & 0 & N_{1,z}\cos n\theta & ... \\ N_{1,z}\cos n\theta & 0 & N_{1,r}\cos n\theta & ... \end{bmatrix} \tag{4.14}$$

and

$$\mathbf{A_2} = \begin{bmatrix} -\left(nN_1/_r\right)\sin n\theta & (N_{1,r} - \left(N_1/_r\right))\sin n\theta & 0 & ... \\ 0 & N_{1,z}\sin n\theta & -\left(nN_1/_r\right)\sin n\theta & ... \end{bmatrix} \tag{4.15}$$

$\mathbf{A_1}$ and $\mathbf{A_2}$ can be written as $\mathbf{A_1} = \mathbf{B_A} \times \mathbf{B_c}$ and $\mathbf{A_2} = \mathbf{B_B} \times \mathbf{B_D}$ where

$$\mathbf{B_A} = \begin{bmatrix} N_{1,r} & 0 & 0 & ... \\ \left(N_1/r\right) & \left(nN_1/r\right) & 0 & ... \\ 0 & 0 & N_{1,z} & ... \\ N_{1,z} & 0 & N_{1,r} & ... \end{bmatrix} \tag{4.16}$$

and

$$\mathbf{B_C} = \begin{bmatrix} 1 & 0 & 0 & \cdots \\ 0 & n & 0 & \cdots \\ 0 & 0 & 1 & \cdots \\ \vdots & \vdots & \vdots & \ddots \end{bmatrix} \cos n\theta$$

$$\mathbf{B_B} = \begin{bmatrix} -(N_1/r) & (N_{1,r} - (N_1/r)) & 0 & \dots \\ 0 & N_{1,z} & -(N_1/r) & \dots \end{bmatrix} \tag{4.17}$$

and

$$\mathbf{B_D} = \begin{bmatrix} n & 0 & 0 & \cdots \\ 0 & 1 & 0 & \cdots \\ 0 & 0 & n & \cdots \\ \vdots & \vdots & \vdots & \ddots \end{bmatrix} \sin n\theta$$

where $\mathbf{B_A}$ and $\mathbf{B_B}$ are independent of n and θ. As a result of the Equation 4.16 and Equation 4.17, one can rewrite the strain-displacement matrix as:

$$\mathbf{B} = \left[\frac{B_A B_C}{B_B B_D}\right] \tag{4.18}$$

The constitutive matrix $\mathbf{E}$ can be partitioned as:

$$\mathbf{E} = \begin{bmatrix} E_{4*4} & E_{2*4} \\ E_{2*4} & E_{2*2} \end{bmatrix} \tag{4.19}$$

The following expression is then obtained:

$$[B]^T [E] [B] = \begin{bmatrix} {B_c}^T {B_A}^T & {B_D}^T {B_B}^T \end{bmatrix} * \begin{bmatrix} E_{4*4} & E_{2*4} \\ E_{2*4} & E_{2*2} \end{bmatrix} * \left[\frac{B_A B_C}{B_B B_D}\right] \tag{4.20}$$

$$\mathbf{K} = \int_{-1}^{1}\int_{-1}^{1}\int_{-\pi}^{\pi} \mathbf{B^T E B} r d\theta \det \mathbf{J} d\xi d\eta \tag{4.21}$$

$$\begin{aligned} &\int_{-1}^{1}\int_{-1}^{1}\int_{-\pi}^{\pi} ({B_C}^T {B_A}^T E_{4x4} B_A B_C + {B_D}^T {B_B}^T E_{2x4} B_A B_C + {B_C}^T {B_A}^T E_{2x4} B_B B_D \\ &+ {B_D}^T {B_B}^T E_{4x4} B_B B_D) r d\theta \det J d\xi d\eta \end{aligned} \tag{4.22}$$

The integrations of the trigonometric terms over the circumference result in:

$$\int_{-\pi}^{\pi} \cos^2 n\theta = \pi \quad \text{if } n \neq 0 \tag{4.23}$$

$$\int_{-\pi}^{\pi} \sin^2 n\theta = \pi \quad \text{if } n \neq 0 \tag{4.24}$$

$$\int_{-\pi}^{\pi} \sin n\theta \cos n\theta = 0 \quad \text{for all } n \tag{4.25}$$

Using the orthogonality properties of the trigonometric functions and performing the circumferential integration, the stiffness matrix becomes:

$$\mathbf{K} = \pi(\mathbf{k_1} + \mathbf{k_2}) \det \mathbf{J} r \quad \text{if } n \neq 0 \tag{4.26}$$

where

$$\mathbf{k_1} = \begin{bmatrix} 1 & 0 & 0 & \cdots \\ 0 & n & 0 & \cdots \\ 0 & 0 & 1 & \cdots \\ \vdots & \vdots & \vdots & \ddots \end{bmatrix} \times \mathbf{k_{11}} \times \begin{bmatrix} 1 & 0 & 0 & \cdots \\ 0 & n & 0 & \cdots \\ 0 & 0 & 1 & \cdots \\ \vdots & \vdots & \vdots & \ddots \end{bmatrix} \tag{4.27}$$

$$\mathbf{k_2} = \begin{bmatrix} n & 0 & 0 & \cdots \\ 0 & 1 & 0 & \cdots \\ 0 & 0 & n & \cdots \\ \vdots & \vdots & \vdots & \ddots \end{bmatrix} \times \mathbf{k_{22}} \times \begin{bmatrix} n & 0 & 0 & \cdots \\ 0 & 1 & 0 & \cdots \\ 0 & 0 & n & \cdots \\ \vdots & \vdots & \vdots & \ddots \end{bmatrix} \tag{4.28}$$

where

$$\mathbf{k_{11}} = \int_{-1}^{1} \int_{-1}^{1} \mathbf{B_A}^T \mathbf{E_{4x4}} \mathbf{B_A} \det \mathbf{J} d\xi d\eta \tag{4.29}$$

$$\mathbf{k_{22}} = \int_{-1}^{1}\int_{-1}^{1} \mathbf{B_B}^T \mathbf{E_{2x2}} \mathbf{B_B} \det \mathbf{J} d\xi d\eta \tag{4.30}$$

In these equations, $\mathbf{k_{11}}$ and $\mathbf{k_{22}}$ are independent of n and θ; therefore, they are computed only once for each Fourier iteration. This property of the stiffness matrix significantly reduces the computational time of large structural problems when many terms of the Fourier series are summed to represent the applied load.

4.2.4 Numerical Time Integration

The explicit time integration method often requires less computational time as compared to the implicit methods [59]. The diagonal mass matrix obtained from the spectral element formulation allows the use of the explicit method. The stable time step is typically recommended as as $^1/_{(20f)}$ where f is the maximum frequency of interest. In this study, the time step is set as $^1/_{(25f)}$ to reduce the influence of time integration to the output waveforms. Reducing the time step does nothave significant influence on the computational time of SEM. In order to show the computational efficiency of the 2D SEM formulation in comparison with the 3D FEM formulation, the unconditionally stable condition average acceleration method is implemented to solve the numerical time integration.

4.3 Verification of the Numerical Formulation

A 3D circular cylinder pipe shown in Figure 12 is modeled using conventional FEM tools in order to verify the numerical formulation. The pipe dimensions are 20 mm thickness, 50 mm radius and 500 mm length. The 3D geometry is meshed with the resolution of $^1/_{(20_{th})}$ of the wavelength using the wave velocity as 3200 $(m)\,(sec)^{-1}$. The 2D geometry, shown in

Figure 13, is divided into square elements using the 4^{th} order Legendre polynomials. The material properties are 200 GPa for Young's Modulus, 7850 $(kg)\,(m)^{-3}$ for density and 0.33 for Poisson's ratio. The comparison is performed using static point load and dynamic three-cycle sinusoidal point load with 10 kHz frequency applied at the edge of the pipe. The other end of the pipe is modeled as the fixed boundary condition. The boundaries along the internal and external walls of the pipe are considered as air/solid/air.

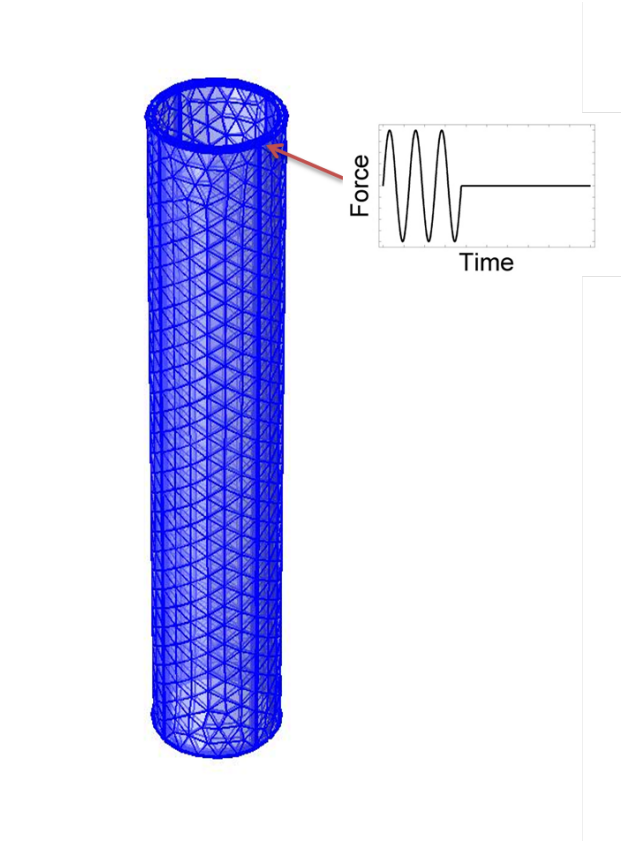

Figure 12: 3D FEM model

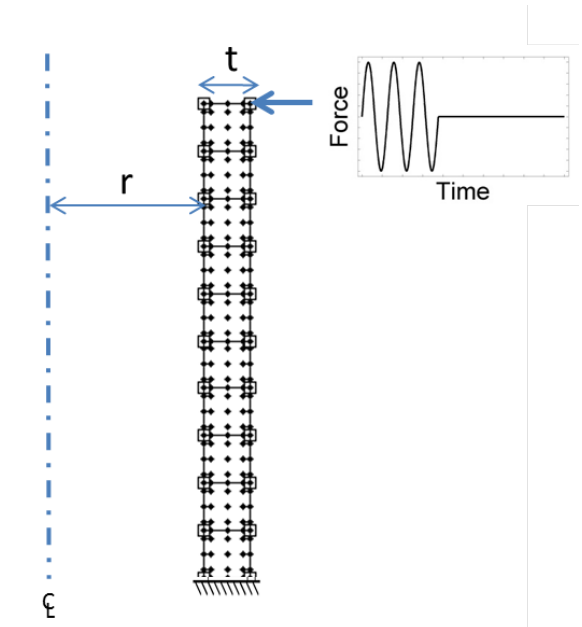

Figure 13: 2D SEM model

The displacement history at the edge of the pipe obtained from the 2D formulation is compared with the result obtained from 3D conventional finite element model in Figure 14. The results of both models match well.

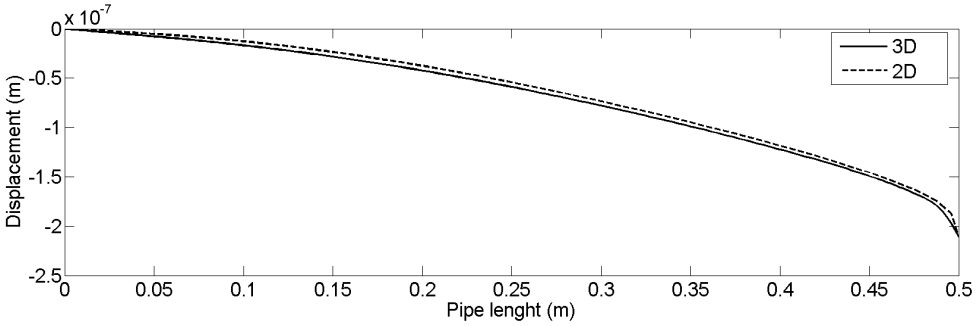

Figure 14: The static displacements along the pipe for the 2D SEM and 3D FEM models models

To validate the numerical formulation under dynamic point load, the displacement histories of the 2D model using presented numerical formulation and the 3D model are compared for three different points along the pipe line as shown in Figure 15.

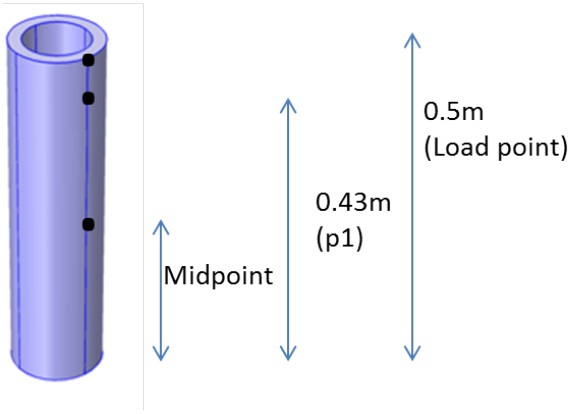

Figure 15: Three measurement points of displacement histories

The displacement histories in radial and axial directions at the loading point for the 2D model and the 3D model using COMSOL software are shown in Figure16(a). Both models agree in time domain and frequency domain. Figure16(b) indicates the peak frequency close to $10kHz$ peak frequency, similar to the excitation frequency. In addition to COMSOL software, the 3D model is solved using ANSYS program as an additional benchmark study. Both programs have different input variables, such as element type and solver method, which influence the output waveform. The element types and time integration of both methods are summarized in Table IV. The element types of COMSOL and 2D models are tethrahedral, and spectral element, respectively. For ANSYS, there are two options: Solid285 (lower order 3D element with four nodes having four degrees of freedom at each node) and Solid187 (higher-order 3D

element having ten nodes and three degrees of freedom at each node). The comparison of ANSYS, COMSOL and 2D model shows that Solid187 results in better agreement with the 2D model and the 3D COMSOL model. While the time integration method of ANSYS and 2D model are the same as Newmark's method, COMSOL has options as generalized alpha and backward differential formulation (BDF). The generalized alpha method is an implicit method which intends to increase the numerical damping without having any effect on the order of accuracy. The BDF method is an implicit multi-step variable-order derivatives method, which is up to the fifth order due to the absolute stability region. As undamped models are not simulated properly with BDF method, the generalized alpha method is selected in this study. The generalized alpha has a variable as high frequency amplification factor in the range of 0 to 1. In this study, the high frequency amplification factor is varied until the COMSOL result fits well with the ANSYS result.

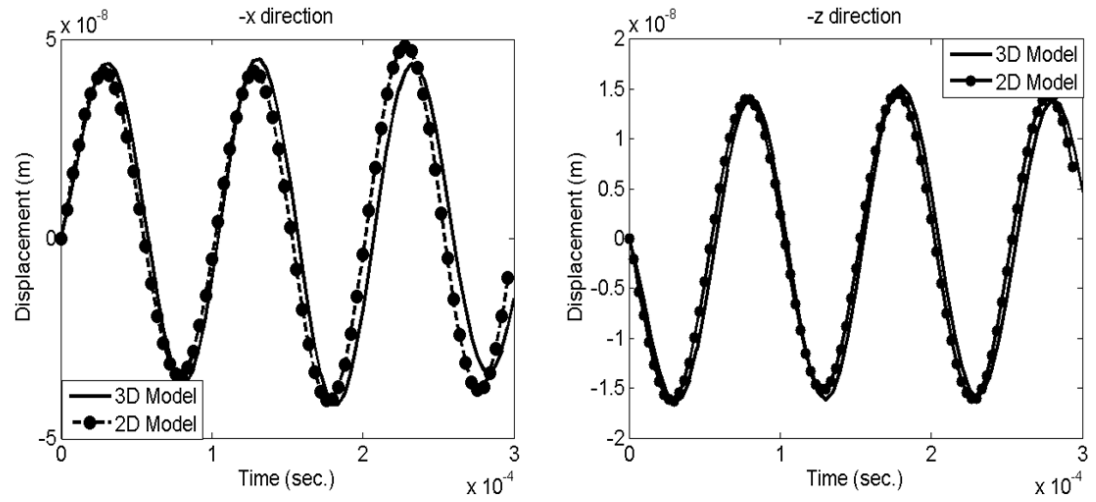

(a)

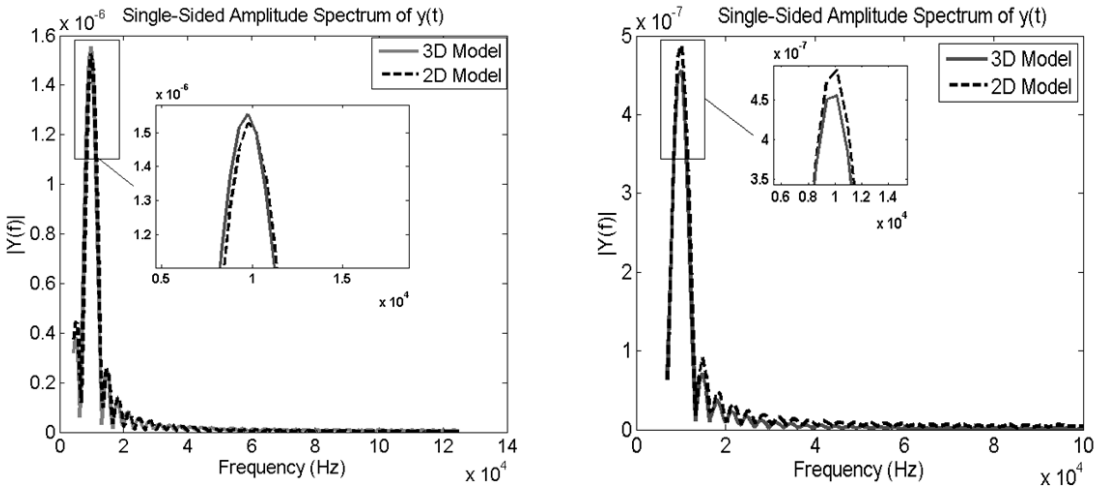

(b)

Figure 16: (a) The displacement historiess at the edge of the pipe for the 2D SEM and 3D FEM (COMSOL) models in radial and axial directions, (b) corresponding frequency spectra of time domain solution

TABLE IV: Element types and time integration methods for COMSOL, ANSYS and 2D model

	3D COMSOL Model	3D ANSYS Model	2D Model
Element Type	Free Tetrahederal	Solid 187	Spectral element (Poly. order 4)
Time Integration Method	Generalized alpha	Newmark's Method	Newmark's Method

The comparison of the axial displacement histories using the 2D and 3D models at the point 1 is shown in Figure 17. Although a good agreement is found between the 2D and 3D ANSYS and COMSOL models, especially the arrival time, magnitude and shape of the first wave cycle, there are slight differences after the second cycle. The differences in element types and time integration methods are considered as the main reasons of slight differences in the solutions of three models. It is worth mentioning that the 2D result relies on the expansion of Fourier series of delta function in the direction which is known as nonconvergent; therefore, the concentrated load is replaced by a narrow rectangular pulse which has an intensity of $(2r_0\theta_0)^{-1}$ over the distance $(2r_0\theta_0)$, where the $2\theta_0$ is a length of small arch [72].

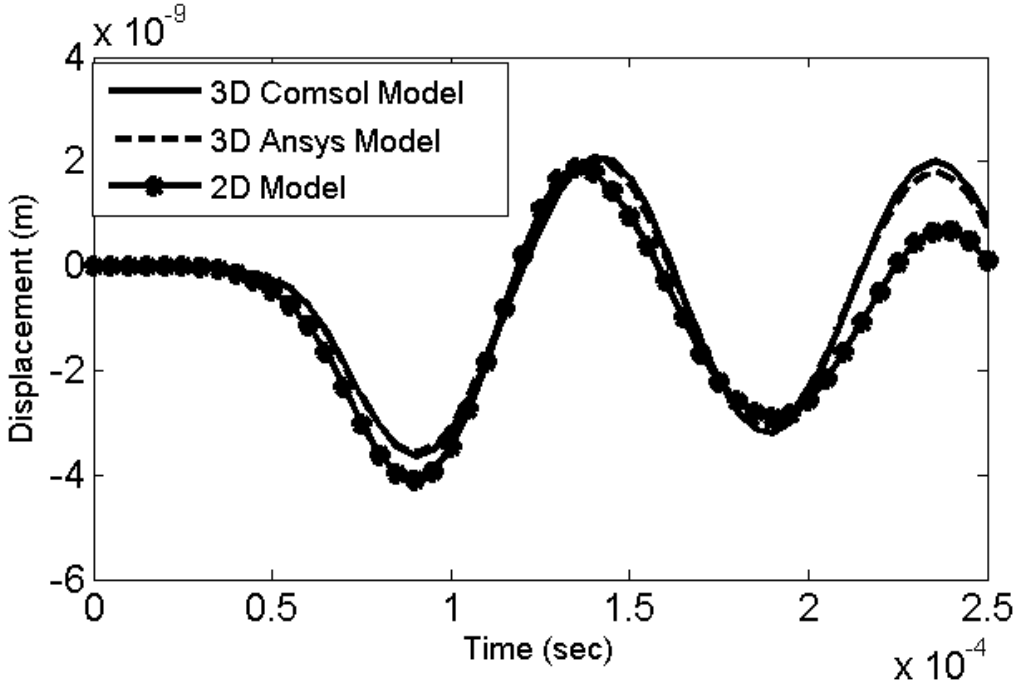

Figure 17: Axial displacement histories of 2D SEM and 3D FEM models (COMSOL and Ansys) at point 1

The comparison of the 2D and 3D models is extended to the radial displacement of further point than the excitation location (i.e., the mid-point), and the result is shown in Figure 18. The 2D model agrees well with the 3D models. The static and dynamic loading results validate the accuracy of the 2D axisymmetric model for non-axisymmetric loading using spectral elements and the method of partitioning of strain-displacement matrix. In next section, efficiency of implementing 2D model formulated in this study is discussed.

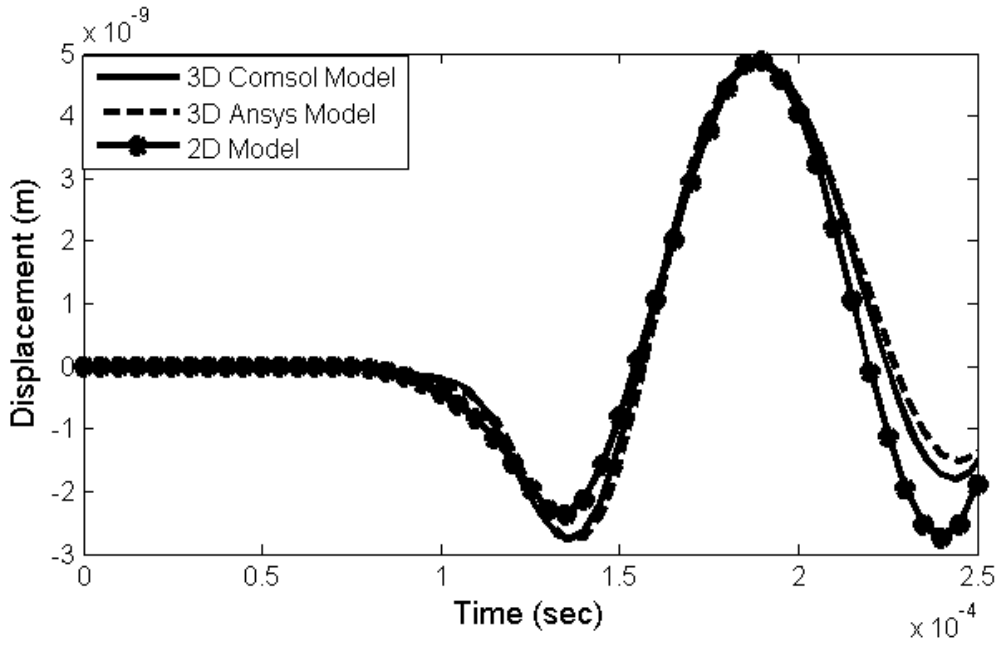

Figure 18: Radial displacement histories of 2D SEM and 3D FEM models (COMSOL and Ansys) at mid-point

4.4 Efficency of 2D Model

There are two fundamental sources that influence the computational time efficiency of the numerical model: extracting mass and stiffness matrices using numerical techniques and performing numerical time integration. The computational time efficiency of the 2D model is controlled by reduction in degrees of freedom to calculate stiffness and mass matrices, decoupling θ (the angular parameter) and n (the number of Fourier terms) from strain-displacement matrix and diagonal mass matrix that enhance numerical time integration. The degrees of free-

dom (dofs) needed for the 2D and 3D (COMSOL) models to reach 10 kHz frequency resolution are 600 and 30885, respectively. There is significant reduction in the dofs when the axisymmetric geometry is taken into consideration, and the spectral element is selected to model the structural domain. The difference between the 2D and 3D models increases dramatically when the required frequency resolution is increased. It is difficult to separate the computational time of the 3D model for the numerical calculations of the mass and stiffness matrices, and the time integration. However, the comparison of overall computational times of the 2D and 3D models shows the efficiency of the 2D model developed in this study. For instance, the difference in the computational time in the 2D model is about 400 seconds when the frequency is increased from 10 kHz to 20 kHz while it is 3000 seconds for FEM. It is recorded that while reducing the time step does not greatly influence the computational time of the spectral element, the computational time increases for the classical finite element formulation.

4.5 Summary

This chapter implements the use of spectral elements for wave propagation, and presents an efficient formulation of the problem of wave propagation along the length of axisymmetric pipes under non-axisymmetric loading. The axisymmetric geometry of the pipe is simplified by reducing the problem to 2D while the non-axisymmetric loading is represented by the summation of Fourier series. The strain-displacement matrix is partitioned in such a way that numerical integration components are decoupled from θ(the angular parameter) and n (the Fourier series terms). The numerical formulation is built using spectral elements. The orthogonal Legendre polynomials are selected to define the nodal points of the discretized finite element. The 2D

numerical model is compared with the 3D model using conventional finite element software, and the accuracy of the 2D model is validated under static and dynamic loading. Because of the numerical integration elements of the stiffness matrix as independent from θ and n, and the diagonal mass matrix resulting from the use of spectral elements, long pipes could be modeled for high frequency wave propagation.

CHAPTER 5

NON-REFLECTIVE BOUNDARY CONDITION MODEL

The content presented in this chapter was previously partially published in the proceeding of the SPIE 2014 conference of Smart Structures/NDE as "High frequency elastic wave propagation in large structures using spectral elements and perfectly matched layer" with my research advisor, Dr. Ozevin, as the co-author [2].

5.1 Introduction

This chapter presents the time-domain, displacement-based Perfectly Matched Layer (PML) equations for plane-stress motion of an isotropic elastic medium. The PML formulations developed by Basu and Chopra [57] are adapted to model an unphysical absorbing layer for the elastic wave equation. By using the special choice of stretching functions, the frequency domain equations are transformed into the time domain. The detailed PML formulations are presented in Appendix A. The experiments were conducted on two steel plates with different lengths in order to validate the numerical formulation. Steel ball drop was selected as the source function. The vertical motions at various positions were recorded using a laser Doppler vibrometer (LDV) and resonant-type piezoelectric AE sensor, which is presented in chapter 6. LDV allows recording true velocities without influencing the data, unlike resonant-type piezoelectric AE sensors.

The organization of this chapter is as follows. The descriptions of numerical and experimental models are presented in Sections 2 and 3, respectively. The comparison of numerical and experimental results on a steel beam is discussed in Section 4. The summary is presented in Section 5.

5.2 Perfectly Matched Layer Formulations

In this study, the PML formulations developed by Basu and Chopra [57] are adapted to model an unphysical absorbing layer in elastic medium. The displacements of such a medium are governed by the following equations:

$$C_{ijkl} \times \bar{\varepsilon}_{kl} = \bar{\sigma}_{ij} \tag{5.1a}$$

$$(\frac{(\bar{\sigma}_{ij})_{,j}}{\lambda_j(x_j)}) = -\omega^2 \rho \bar{u}_i \tag{5.1b}$$

$$\bar{\varepsilon}_{ij} = [\frac{\bar{u}_{i,j}}{\lambda_j\,(x_j)} + \frac{\bar{u}_{j,i}}{\lambda_i\,(x_i)}]/2 \quad no\ sum \tag{5.1c}$$

where ω denotes the frequency of excitation and λ_j are stretching functions. $\bar{\sigma}_{ij}$,$\bar{\varepsilon}_{kl}$, $\bar{u}_i$ are the components of $\bar{\sigma}$,$\bar{\varepsilon}$, $\bar{\mathbf{u}}$, the stress, infinitesimal strain and displacement tensors as a harmonic time-dependent variable, such as $\mathbf{u}\,(x,t) = \overline{\mathbf{u}}(x)e^{i\omega t}$. C_{ijkl} are the components of the material stiffness tensor, and defined as:

$$C_{ijkl} = k\delta_{ij}\delta_{kl} + \mu(\delta_{ik}\delta_{jl} + \delta_{il}\delta_{jk} - {}^{2}\!/_{3}\delta_{ij}\delta_{kl}) \tag{5.2}$$

where k is the bulk modulus and μ is the shear modulus.

Although there is no exact technique suggested in the literature for choosing the stretching function, the proper choices of λ_i lead to the attenuated wave solutions in the direction of propagation. When the inverse Fourier transform is essential to obtain time domain equation, it is suitable to choose the stretching function λ as a simple function of ω [46]:

$$\lambda_i\left(x'_i\right) := \left[1 + {f_i}^e\left(x'_i\right)\right] - i\frac{{f_i}^p\left(x'_i\right)}{k_s} \tag{5.3}$$

where k_s is the wavenumber and the functions ${f_i}^e$, ${f_i}^p$ tend to attenuate evanescent and propagating waves, respectively.

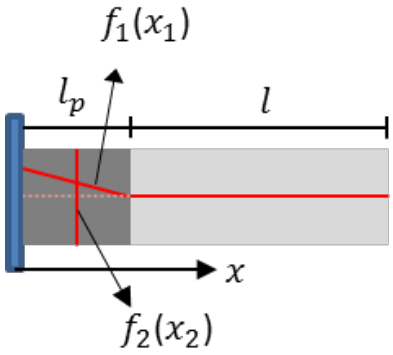

Figure 19: One-dimensional PML model with stretching functions

Figure 19 shows one-dimensional PML model implemented in this study where the linear attenuation functions are chosen as ${f_i}^e = {f_i}^p = f_i$, with $f_1(x_i)$ is defined in Equation 5.4 and$f_1(x_i) = 0$;

$$f := 0.05(\frac{((l - |x| + |l - |x||)}{2})/l_p \tag{5.4}$$

where l is the depth of physical domain and l_P is the depth of PML.

5.3 Experimental Design

The purpose of the experiments is to validate the numerical simulations. A photograph and a simplified schematic of the overall experimental setup are shown in Figure 20. Two steel plates with the lengths of 300 mm and 600 mm and thickness of 9.5 mm were utilized to study the boundary effect to the received signal characteristics. One edge of the plate was fixed using a clamp; the other end was free to represent natural boundary condition. The out of plane velocities at various positions along the plates were measured using PDV-100 digital vibrometer, which was connected directly to a digital oscilloscope (MSO2014 oscilloscope with 100 *MHz* bandwidth and 1 *Gbps* sample rate). The PDV detects true surface velocity based on the transduction principle of laser interferometer within the frequency range of 0-22 *kHz*. The experiments were repeated using 60 *kHz* resonant-type piezoelectric sensor to study the influence of piezoelectric transduction to the AE features.

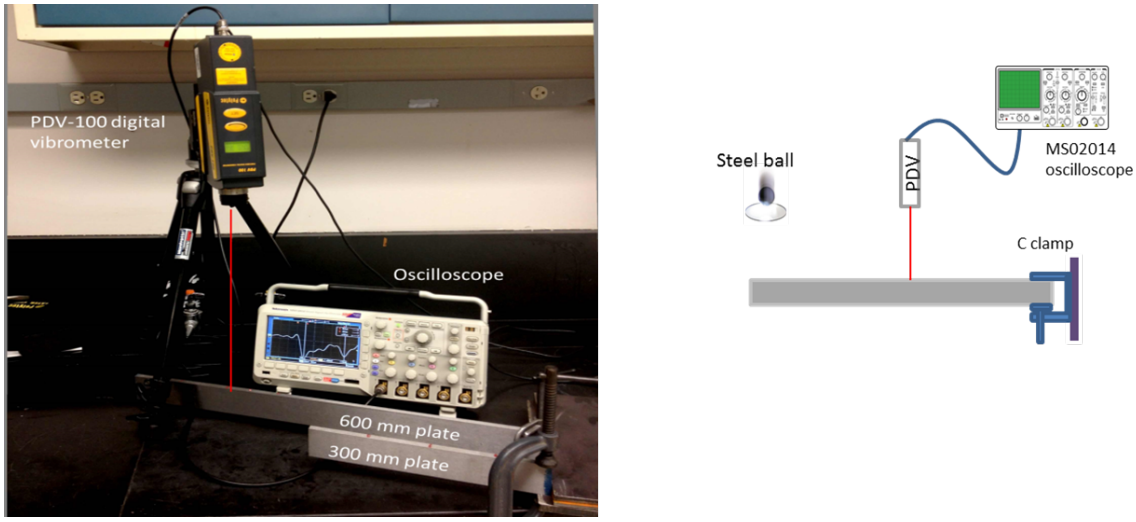

Figure 20: Experimental setup

A steel ball drop was selected as the simulation source, Figure 20. The specifications of the steel ball drop are 11 mm diameter ball and 56 mm drop height. The force function generated by ball drop on a material is obtained by Equation 5.5 and Equation 5.6, using impact theory [87] and plotted in Figure 21. The equations are based on elastic contact theory between steel ball and plate, and do not include the bouncing effect. A thin layer of grease was applied to the plate surface to prevent the bouncing in experiments. The force function shown in this figure is utilized as the excitation source for the numerical model.

$$F = \frac{1.14 m \vartheta_0^2}{\alpha_m} \sin\left(\frac{1.068 \vartheta_0 t}{\alpha_m}\right); \quad \text{for} \quad 0 \leqslant t \leqslant \frac{\pi \alpha_m}{1.068 \vartheta_0} \tag{5.5}$$

$$F = 0 \quad \text{for} \quad t \geqslant \frac{\pi \alpha_m}{1.068 \vartheta_0} \tag{5.6}$$

where m is the ball mass, α_m is the impact parameter and defined by

$$\alpha_m = (\frac{15\pi \vartheta_0^2 \left(\delta_1 + \delta_2\right) m_1}{16\sqrt{R_1}})^{0.4} \tag{5.7}$$

where $\delta = \frac{1-v}{\pi E}$ calculated from Hertzian contact theory is relative to Poisson's ratio, ν, and inverse of Young's Modulus, E, and R is radius. The initial relative velocity at free fall is $\vartheta_0 = \sqrt{2gH}$ where g is the gravity constant and H is the height of fall.

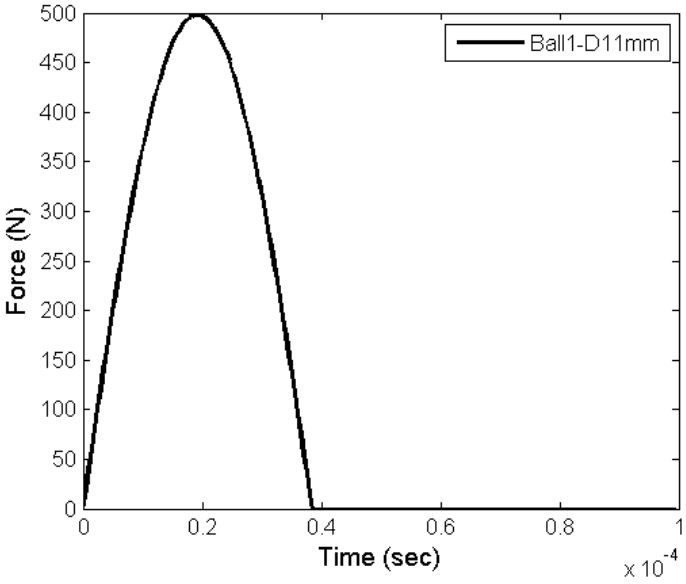

Figure 21: Source function of 11 mm diameter ball drop from 56 mm height

5.4 The Validation of the Numerical Models

The numerical models similar to the experimental geometry and boundary conditions were built, and compared with the experimental results using the PDV. The vertical surface velocity was measured from a point on each plate as shown in Figure 22. The 300 *mm* long plate is called as case-1; the 600 *mm* long plate is called as case-2.

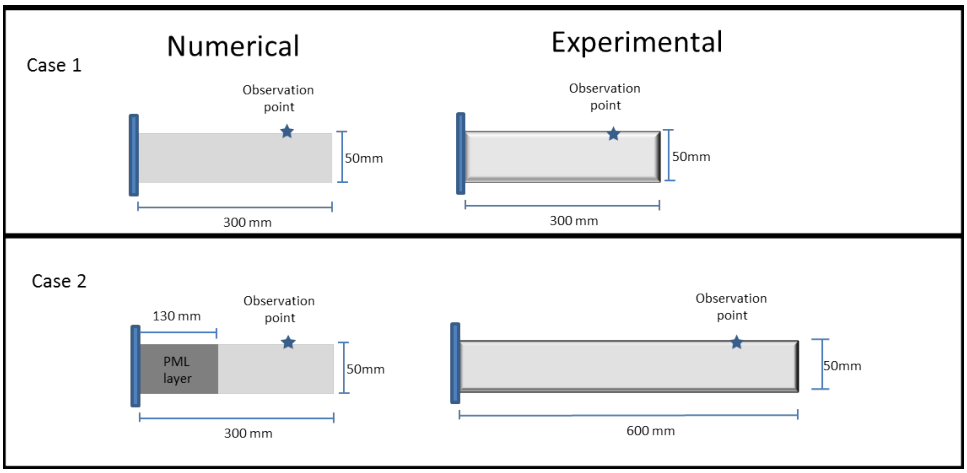

Figure 22: Numerical and experimental geometries and boundaries to measure the velocity at the observation point

Numerical models were constructed for two cases as follows: 300 *mm* long plate with fixed boundary condition at the left end of the plate simulating case-1, and 300 *mm* long plate with

PML at the left end of the plate simulating case-2. The use of absorbing boundary condition reduces the computational time as compared to modeling 600 mm long plate with the fixed boundary condition. The advantage of PML boundary becomes especially pronounced if a particular high frequency excitation is simulated where wavelength becomes smaller, and the required PML domain length becomes shorter; on the other hand, degrees of freedom for full model would increase significantly with shorter wavelength to reach to accurate solution (note that minimum mesh size should be $1/20^{th}$ of wavelength for dynamic finite element). Young's Modulus, density and Poisson's ratio of the steel plate selected for the plane stress numerical model are E=200 GPa, ρ=7850 $(kg)\,(m)^{-3}$ and ν=0.3, respectively. The spectral element model includes 20-element, 5-node per direction polynomial mesh, leading to 6560 degrees of freedom. There is no change in the degrees of freedom for the numerical model with the PML boundary, as the total length of physical and PML domains is the same at 300 mm. The total length of the numerical model with the PML boundary is divided into two domains: 170 mm for the physical domain and 130 mm for the PML domain.

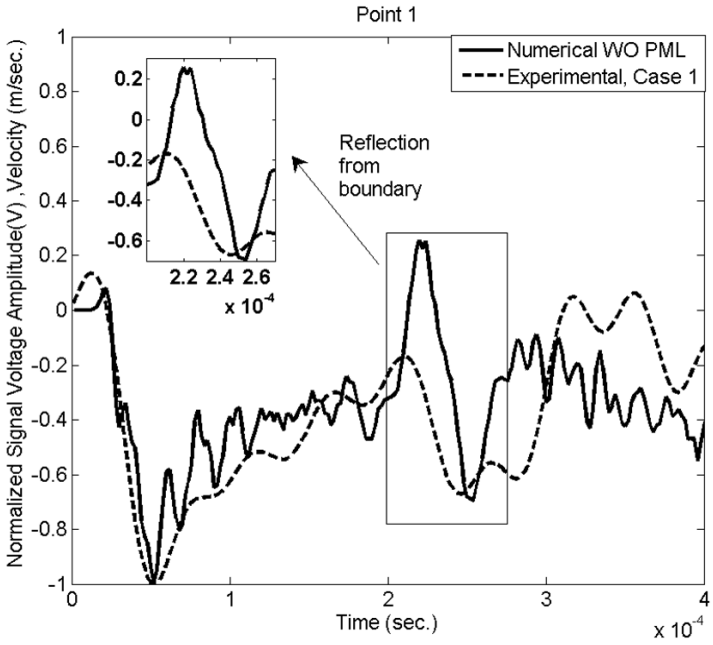

(a) Numerical model without PML versus case 1 experimental result

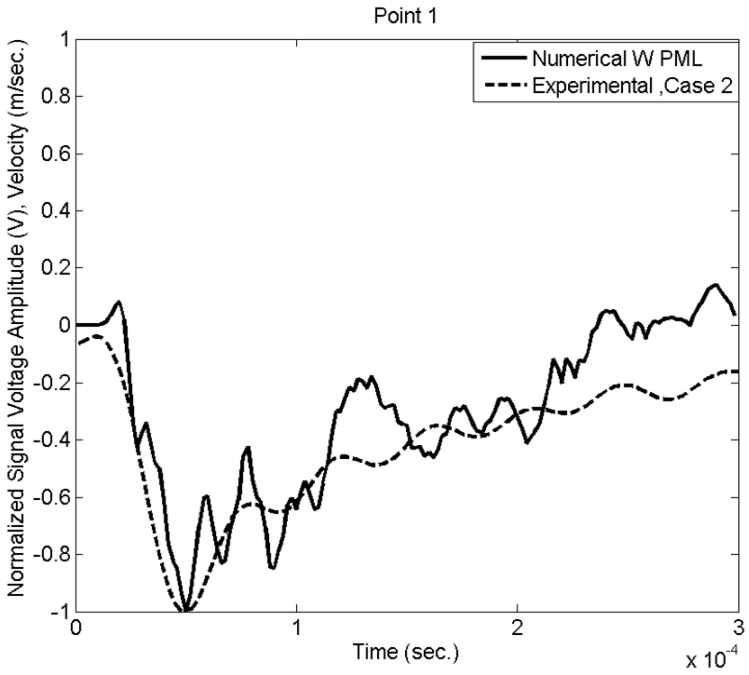

(b) Numerical model with PML versus case 2 experimental results

Figure 23: The velocity history in -y direction at the measurement point

Figure 23 compares the velocity histories of the numerical model with/without PML boundary conditions and the experimental results. The reflection from the fixed boundary for case-1 occurs about 200 μs as illustrated in the inset plot of Figure23(a). Numerical and experimental results agree very well especially at the first pulse arrival. The relative magnitude of the reflected wave with respect to the initial pulse depends on the acoustic impedance of the boundary. The numerical model considers an ideal fixed boundary condition while in reality the boundary condition is not fully fixed. Therefore, the reflected wave magnitude is slightly higher for the numerical model as compared to the experimental result. Figure 23(b) shows the comparison of the longer plate result (case-2) and the numerical model with the PML boundary. The boundary reflection disappears at 200 μs from both numerical model and experimental result. The numerical model has higher frequency oscillations as compared to the experimental result. The PDV has limited bandwidth as 0-22 kHz; therefore, higher frequencies cannot be detected. Considering uncertainties in measurement, assumptions and simplifications in numerical models, experimental and numerical results are considered to be in good agreement.

5.5 Summary

In this chapter, the displacement-based, time-domain PMLs along with spectral element formulations are described in order to investigate the influence of boundary reflections on the elastic wave properties at the receiving points. Experimental and numerical models were constructed for two cases. The velocity histories of the numerical model with/without PML boundary conditions are compared to the experimental results. Once the PML formulation is validated, the

structural models are formulated for higher frequency source functions, which are presented in the following chapter.

CHAPTER 6

THE INFLUENCE OF BOUNDARY REFLECTION AND SENSOR TRANSFER FUNCTION TO THE AE FEATURES

The content presented in this chapter was previously partially published in the proceeding of the SPIE 2014 conference of Smart Structures/NDE as "High frequency elastic wave propagation in large structures using spectral elements and perfectly matched layer" with my research advisor, Dr. Ozevin, as the co-author [2].

6.1 Introduction

In this chapter, the influences of boundary reflections and piezoelectric sensors on the detection of propagating elastic waves emitted from newly formed damage surfaces are demonstrated using numerical and experimental models. The concepts of the displacement-based, time-domain equations of non-splitting perfectly matched layer (PML) and spectral finite elements are utilized to facilitate computationally efficient modeling for high frequency wave propagation in large scale structures. The boundary reflections within small-scale-coupon specimens modify the received wave characteristics in such a way that transferring the laboratory-scale data to other geometries for pattern recognition methods becomes a challenge. The features used in the pattern recognition algorithms cannot be scaled up to large scale structures unless the experimental geometry is designed through considering the target wavelength, the waveform record-window is limited to prevent the influence of reflected waves and the transfer function

of the piezoelectric sensor is taken into account. A model based on selecting the sample size as a function of wavelength is developed. The influence of piezoelectric sensors to the output signals is demonstrated such that the selected piezoelectric sensor controls the waveform features, which further limits the test repeatability under different conditions. The organization of this chapter is as follows: The influence of boundary reflections on the AE features in relation to the excitation frequency is are presented in Section 2. The influence of piezoelectric sensor on the AE signal is discussed in Section 3. The summary is presented in Section 4.

6.2 The Influence of Reflected Waves to the Received Elastic Wave Characteristics

The reflected waves from boundaries cause complex waveform characteristics at the receiving points. The complexity of the waveform characteristics leads to challenge of applying the results of the small coupons to large scale structures. In order to demonstrate the influence of boundary reflections to the AE characteristics, a 2D plate structure in plane stress condition is modeled with the fixed boundary and the PML boundary under the same excitation source. The frequency of the excitation source is varied as 60 kHz, 100 kHz and 200 kHz (the most common frequencies of the AE sensors used for engineering applications). Figure 24 shows the plate geometry and two boundary conditions modeled. The length of PML domain is varied depending on the wavelength of the target frequency. In this study the PML lengths of 37 mm, 30 mm and 25 mm are considered for 60 kHz, 100kHz and 200 kHz, respectively. Structural damping is not considered.

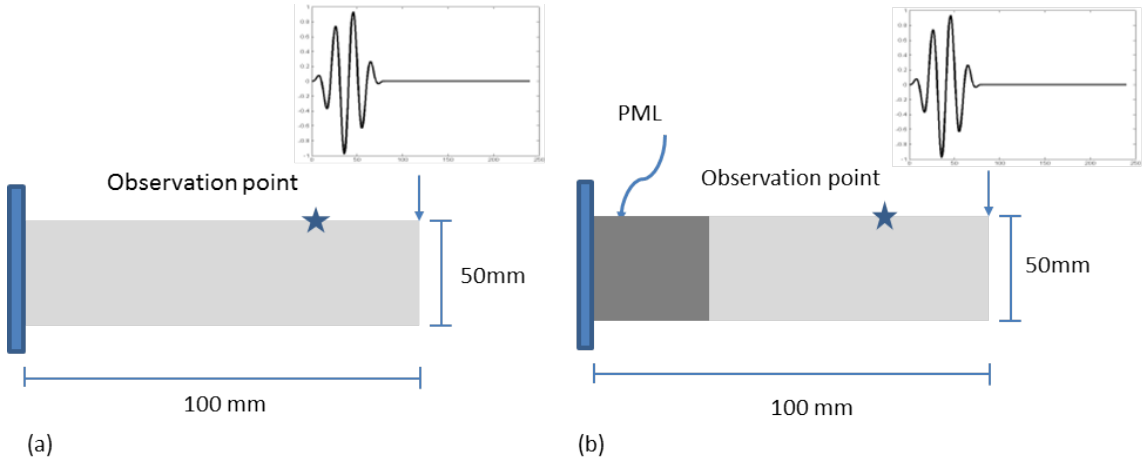

Figure 24: Numerical models with (a) fixed boundary condition, (b) absorbing boundary condition

The vertical displacements at the observation point for three frequencies with (W) and without (WO) PML domain are presented in Figure 25. The first wave envelope is identical for both models while the reflected waves from the fixed boundary (WO PML cases in the figure) clearly modify the AE characteristics including duration, energy, count etc.

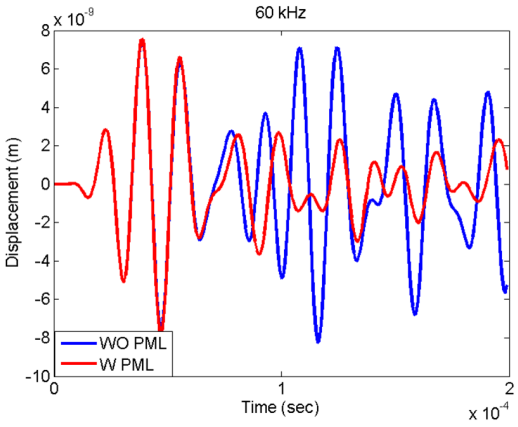

(a) 60 *kHz*

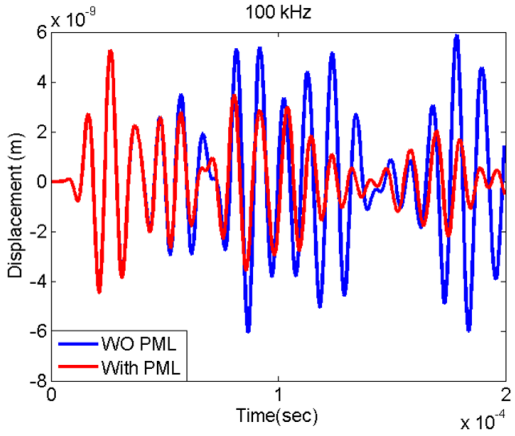

(b) 100 *kHz*

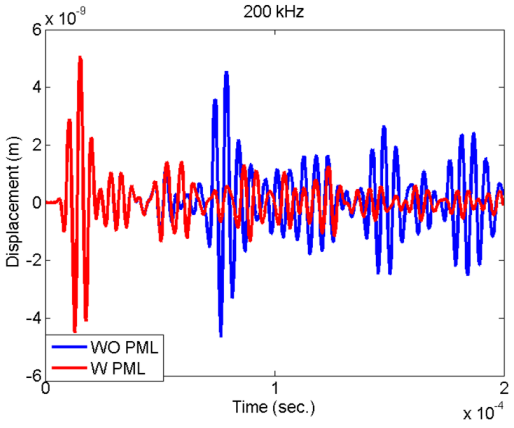

(c) 200 *kHz*

Figure 25: Displacements of an observation point, numerical model without PML versus with PML for 60, 100 and 200 *kHz*

In addition to the time domain AE features, the frequency domain features are also influenced by the reflected waves as shown in Figure 26. The peak frequencies change as well as their spectrum energies and distributions along the spectrum, which are typically defined as partial powers. For instance, the peak frequency for 60 kHz excitation with the fixed boundary is 45 kHz while the peak frequency for 60 kHz excitation with the PML boundary is 69 kHz (closer to actual excitation frequency).

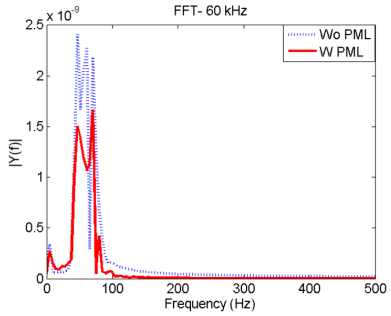

(a) 60 kHz

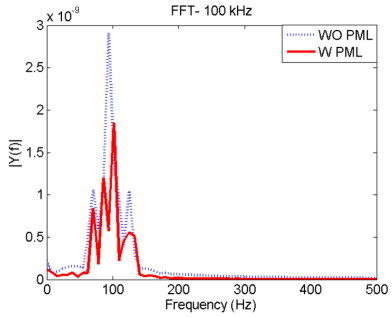

(b) 100 kHz

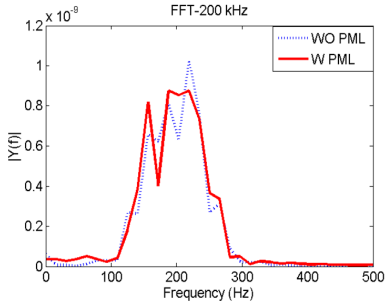

(c) 200 kHz

Figure 26: Frequency spectra of vertical displacements at the observation point for numerical model without PML versus with PML for 60, 100 and 200 kHz excitation frequencies

TABLE V: The comparison of AE features with and without PML domain

AE feature	60kHz		100kHz		200kHz	
	WO PML	W PML	WO PML	W PML	WO PML	W PML
Maximum Amplitude (m)	7.47E-9	7.54E-9	5.90E-9	5.26E-9	5.08E-9	5.08E-9
Duration (μs)	1.73E-4	1.78E-4	1.85E-4	1.64E-4	1.83E-4	1.14E-4
Energy (m-s)	2.77E-13	1.66E-13	2.02E-13	1.04E-13	8.9E-14	4.2E-14
Peak Frequency (kHz)	45.7	69.14	91.8	99.61	175.8	183.6
Frequency Centroid (kHz)	101.67	63.83	130.865	97.77	206.23	206.54

The extracted time and frequency domain features of two models for three frequencies are summarized in Table V. The threshold level to calculate time domain features is selected as $1 \times 10^{-9} m$. The time domain features especially energy increase with the boundary reflections. When the frequency goes down, the boundary reflection becomes more influential to the AE characteristics in the frequency domain. This is interpreted as that the experimental geometry should be selected based on the target AE frequency of interest. Otherwise, the AE features extracted from small-coupon specimens cannot be adapted to large scale structures unless the waveform record-window is limited to prevent the boundary reflection reaching to the sensing element during the selected record-window. Figure 27 shows the ratios of the frequency domain features for the bounded and unbounded geometries with respect to wavelength/specimen size. When the wavelength/size approaches 0.1, the difference between the bounded and unbounded geometries becomes smaller.

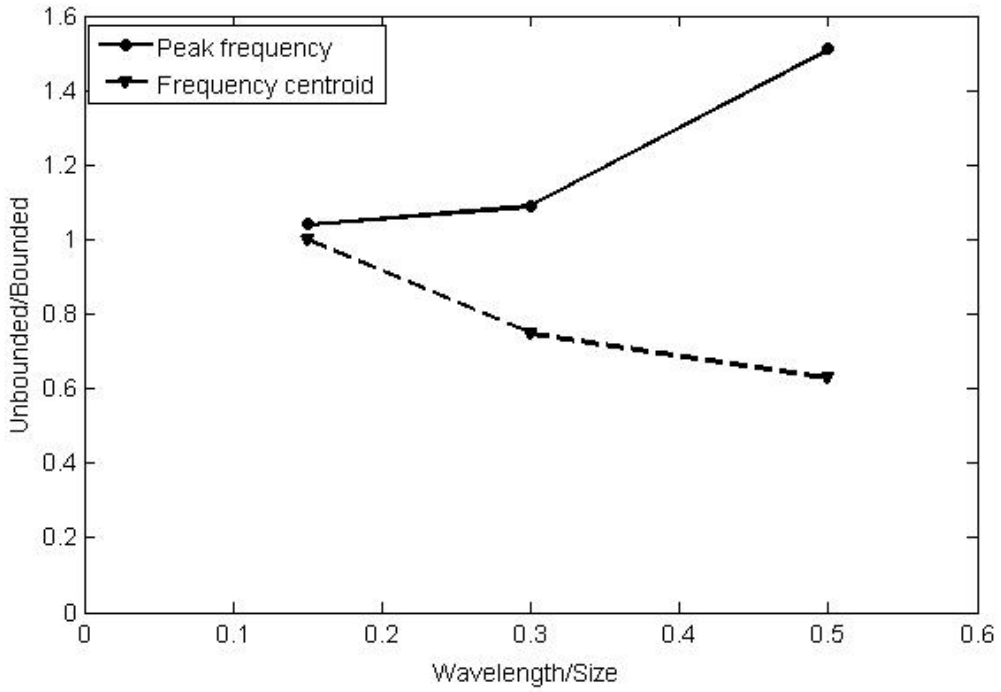

Figure 27: The influences of unbounded and bounded domains on the frequency domain features

6.3 The Influence of Piezoelectric Sensor to the Received Elastic Wave Characteristics

The most common sensor types selected for the AE testing are made of piezoceramics, which are special types of piezoelectric materials. The sensing piezoelectric equations neglecting the temperature effect are [88]:

$$S_{ij} = s^D_{ijkl} T_{kl} + g_{kij} D_k \tag{6.1}$$

$$E_i = g_{ikl} T_{kl} + \beta_{ik}^{T} D_k \tag{6.2}$$

where S_{ij} and T_{kl} are the strain and stress, E_i and D_k are the electric field and electric displacement, the coefficient s_{ijkl} represent stress per unit strain (compliance), the coefficient g_{ikl} is the piezoelectric voltage coefficients. The finite element solution of the wave propagation problem has dependent variable as S_{ij} at the location of the piezoelectric sensor, which is typically assumed as fully coupled to the structure. Using the coefficient matrices of the selected piezoelectric sensor, the output electric field can be determined using Equation 6.1 and Equation 6.2.

The piezoelectric sensors are the last component of recording the AE signal, and they influence the output signal significantly. The geometry, design, finite aperture, and material properties of piezoelectric sensors form a complex system for analytical modeling. The influence of piezoelectric sensor to the received elastic wave characteristics can be addressed through obtaining absolute calibration of the sensor [39], or multi-physics models that consider structural mechanics and piezoelectric models simultaneously [89, 90]. In this study, the piezoelectric equations coupled with structural mechanics as shown in Equation 6.1 and Equation 6.2 are solved using multi-physics simulation tool provided by COMSOL Multiphysics software.

The finite dimension of piezoelectric sensor requires a full 3D modeling approach as shown in Figure 28. A steel plate with the dimensions of 600 $mm\times$ 50 mm and thickness of 9.5 mm is selected to attach the AE sensor. The geometries of the selected transducer element (R6 manufactured by Mistras Group Inc), brass mass at the back surface and aluminum oxide wear plate are coupled with structural model of the steel plate, Figure 10. The material properties

of each layer of the AE sensor are shown in Table VI. The simulation method is steel ball drop, similar to Figure 21. The drop height and ball diameter are selected as 300 mm and 32 mm, respectively, in order to be able to catch the steel ball before bouncing.

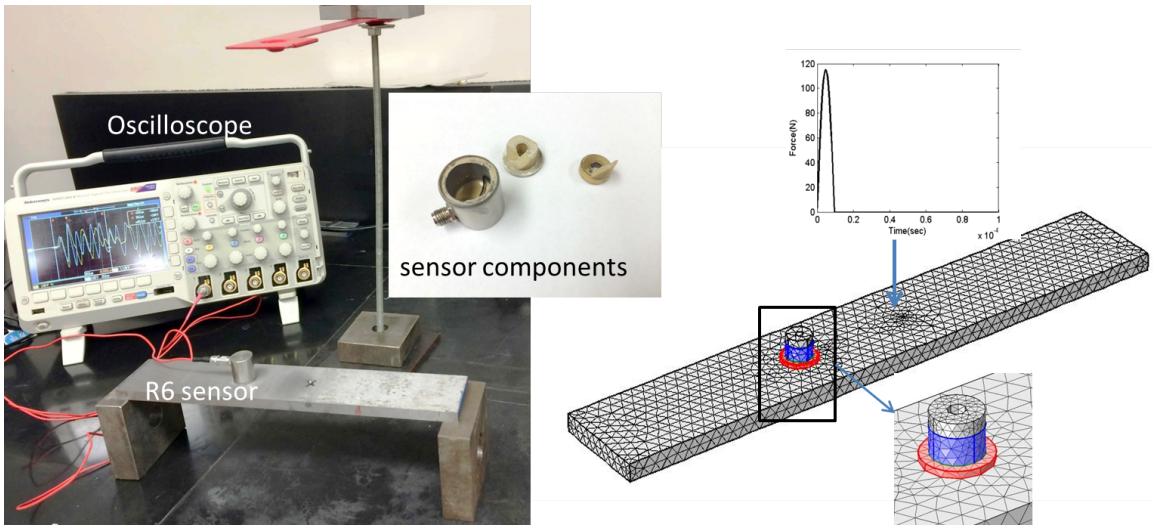

Figure 28: Experimental setup and numerical model

TABLE VI: Elastic and piezoelectric properties of the materials implemented in simulations

Property	PZT-5A	Al_2O_3	Brass
Elastic Modulus (GPa)	C11=C22=121, C12=75.4, C13=75.2, C33=111.2, C66=22.6, C44=C55=21.1	400	105
Density (kg/m^3)	7750	3965	8500
Poisson ratio	0.3	0.22	0.34
Piezoelectric constants C/m^2	S31=S32= –5.4, S33=15.8, S24=S14=12.3		

The vertical surface displacement right underneath the piezoelectric sensor obtained from the numerical model is shown in Figure 29(a). The maximum surface displacement reaches 6×10^{-8} m for the selected time window of 100 μs. The surface motion is converted into electrical signal through the piezoelectric sensor, and Figure 29(b) compares the numerical (gray,

dashed line) and the experimental (black, solid line) outputs of the piezoelectric sensor. The waveform signatures of the models follow the same pattern. The signal voltage obtained from the numerical model is the averaged voltage over the electrode area. The voltage magnitude of the numerical model is about five times higher than the experimental result. The repeated experiments showed that the magnitude depends on many variables such as couplant thickness, type, surface condition of ball drop location etc. The approximations in the source function representing the ball drop impact, the sensor couplant, and material properties make simulating exact experimental conditions in the numerical model difficult. Considering all the variables, the numerical result agrees well with the experimental result.

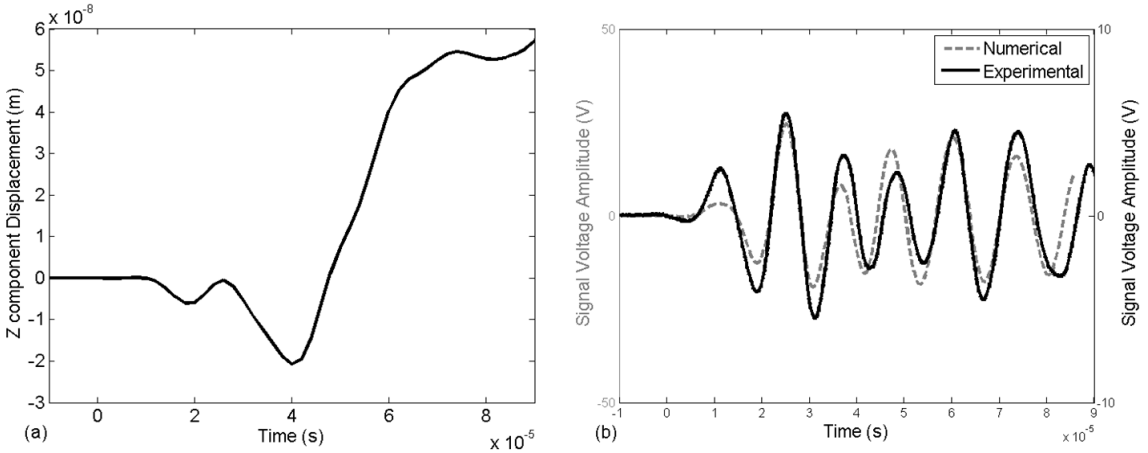

Figure 29: The comparison of numerical and experimental results, (a) surface displacement at the location of the sensor obtained from the numerical model, (b) voltage output obtained from the numerical and the experimental results

The comparison of actual surface displacement and sensor output clearly shows the influence of sensor transfer function on the AE waveform. All the time domain and frequency domain features are influenced by the AE transducer such that the patterns observed in a laboratory condition cannot be repeated unless the same sensor type is selected.

6.4 Summary

This chapter shows the complexity of recording the AE signals related to the propagating wave medium and the sensing element. Because the boundary reflections and the piezoelectric sensor selected in testing modify the output signal significantly, the repeatability of the AE results from one test condition to another becomes a challenge. The changes in structural geometry or sensor type vary the output signal characteristics such that the damage patterns obtained from a specific test condition cannot be repeated in another test condition. The numerical models offer a significant potential to tackle the problem of repeatability. In this chapter, the numerical formulation based on spectral elements and absorbing boundary layers for modeling large scale structures is presented for a computationally efficient formulation. If the sample size is selected appropriately based on the target frequency of interest and the reflected waves are eliminated from the waveform windows, adapting the scaled experimental results to other structures becomes feasible. Complete numerical modeling including the propagating medium and the piezoelectric sensor are needed for quantitative AE. However, modeling the source function is still an ongoing research problem, especially in composite structures.

CHAPTER 7

CONCLUSIONS AND FUTURE WORK

7.1 Conclusions

The general purpose behind the research presented in this thesis is to understand the quantitative significance of the AE signatures through effective numerical models combining the components of source, structure and sensor into the model. The structure model includes spectral element based finite element design and absorbing boundary conditions for modeling elastic wave propagation in large scale structures using sub-scale finite element models. The mathematical formulation of finite elements using the spectral elements allows modeling high frequency wave propagation effectively. The ultimate goals are to predict the waveform signature due to different damage modes for quantitative AE using numerical models, scale the experimental results to different geometries and sensors, and apply real time pattern recognition methods to detect the presence of damage in the midst of high background noise generated by the structural motion. Based on the summary of the approach presented in Chapter 1, the followings are the main conclusions of this study:

- Literature review: There are numerous studies in the literature for obtaining the AE features of different damage modes using coupon samples. The limitation of these studies is that the results cannot be transferred to larger scale geometries or different sensor types. An approach based on numerical models including all the components of the AE method

is needed to address the scalability challenge and modify the method from qualitative to quantitative.

- Spectral element formulation: The selection of the spectral element approach to model the elastic wave equation significantly reduces the required degrees of freedom to reach an accurate solution for high frequency excitation. It is important to determine the polynomial order of the orthogonal function that defines the nodal coordinates of the Lagrangian shape function, and the maximum element size needed for the numerical solution. It is found that as a general approach, to formulate the spectral element model, the average of 16 nodes per wavelength provides sufficient accuracy.This founding can be used to identify the element size based on the selected order of polynomial.

- The application of the spectral element approach to a case study: The AE method is successful for monitoring and detecting leaks in pipelines. The main question is how to determine the spacing between the AE sensors for reliable leak detection. Numerical methods can be used for predicting the attenuation curve for different pipeline geometries. However, 3D modeling of long-range pipeline is computationally expensive. A novel formulation of the wave propagation problem with 2D axisymmetric elements combined with Fourier series summation of non-axisymmetric load function is developed. First, 2D axisymmetric geometry is modeled with spectral elements. Second, "the strain-displacement matrix is partitioned in such a way that numerical integration components are decoupled from θ (the angular parameter) and n (the number of Fourier terms)" [3]. Long-range pipe structures are modeled to identify the sensor spacing.

- Understanding the influence of boundary reflections on the AE features: The challenge of modeling large scale geometries is addressed through combining the spectral element formulation and absorbing boundary conditions to model the wave equation. The comparison of bounded and unbounded domain results shows that the reflections from boundaries influence the AE features leading to a challenge of transferring data from small-scale to large scale. A model based on selecting the sample size as a function of wavelength is developed.

- Understanding the influence of piezoelectric sensor on the AE features: The most common AE sensors are made of piezoelectric materials. The multi-physics simulations and experimental results show that the transfer function of the AE sensor influences the AE signal significantly. Therefore, for the quantitative AE approach, the sensors should be a part of the numerical model for fully autonomous, real time pattern recognition.

7.2 Future work

The future work suggested by this study includes the following:

- The numerical models using the spectral element formulation will be expanded into 3D geometries for studying the wave propagation in complex geometries;

- Distorted geometries such as holes and existing damage will be added to the models to understand the local geometric variables affecting the propagating elastic waves;

- In the present study, the material is considered as homogenous and isotropic. The influence of the localized inhomogeneity and anisotropy on the characteristics of the AE signals will be studied;
- The source models using fracture mechanics will be developed to understand the influence of source mechanisms on the AE signals;
- There are voluminous studies in the literature that implement specific geometry, material and instrumentation to understand the waveform characteristics of damage modes. The challenge is to observe similar patterns in a different laboratory environment with different geometry and instrumentation while the material and the expected damage modes are the same. In future work, a generalized modeling of structures that will encompass each stage of complex data collection will be formed in such a way that the data recorded in one test condition can be transformed into different test conditions.

APPENDICES

Appendix A

PML DETAILED FORMULATION

The equations presented here are based on these references [46, 56, 57].

The strong form of governing equation for homogeneous isotropic elastic medium plain strain can be written as:

$$(C_{ijkl} \times \varepsilon_{kl})_{,j} = \rho\, \ddot{u}_i \tag{A.1a}$$

$$\varepsilon_{ij} = (u_{i,j} + u_{j,i})/2 \tag{A.1b}$$

where indices *i, j, k, l* can be 1 or 2 with the Einstein convention of implicit summation for repeated index, u is the displacement, ρ is the density and $\mathbf{C}$ is defined as:

$$C_{ijkl} = k\delta_{ij}\delta_{kl} + \mu(\delta_{ik}\delta_{jl} + \delta_{il}\delta_{jk} - {}^{2}\!/_{3}\delta_{ij}\delta_{kl}) \tag{A.2}$$

where k is the bulk modulus and μ is the shear modulus.

Equation A.1 admits plane-wave solutions of the form

$$\mathbf{u} = \mathbf{A}exp[-i\,(\mathbf{k}.\mathbf{x} - \omega t)] \tag{A.3}$$

Appendix A (Continued)

where **A** is the amplitude and polarization vector, ω denotes angular frequency, **x** is the position vector and **k** represents the wave vector with Cartesian components k_x, k_y and k_z. For plane P waves:

$$\mathbf{A} \times \mathbf{k} = 0 \tag{A.4}$$

$$k = ({k_x}^2 + {k_y}^2 + {k_z}^2)^{\frac{1}{2}} = \omega / c_p$$

For plane S waves

$$\mathbf{A} \cdot \mathbf{k} = 0 \tag{A.5}$$

$$k = \omega / c_s$$

where c_p, c_s denotes P-wave velocity and S-wave velocity respectively. The Perfectly matched medium is defined to be a medium where the transvers coordinate x is mapped onto the complex coordinate $\widetilde{x}$ with the imaginary part increasing slowly as the wave propagates to the layer [91]. The complex space variable in perfectly matched medium defined as [56]:

$$\widetilde{x_i} := \int_0^{x_i} \lambda_i (s)\, ds \tag{A.6}$$

Appendix A (Continued)

where λ_i is non-zero, continuous stretching function. Let's consider the displacement, stress and strain as a harmonic time dependent variable e.g. $\mathbf{u}(x,t) = \overline{\mathbf{u}}(x)e^{i\omega t}$, the PML formulation for plane-stress dynamic motion in the frequency domain defined as:

$$C_{ijkl} \times \bar{\varepsilon}_{kl} = \bar{\sigma}_{ij} \tag{A.7a}$$

$$(\frac{(\bar{\sigma}_{ij})_{,j}}{\lambda_j(x_j)}) = -\omega^2 \rho \bar{u}_i \tag{A.7b}$$

$$\bar{\varepsilon}_{ij} = [\frac{\bar{u}_{i,j}}{\lambda_j\,(x_j)} + \frac{\bar{u}_{j,i}}{\lambda_i\,(x_i)}]/2 \quad no\ sum \tag{A.7c}$$

For generality, consider the arbitrary orthogonal coordinate system $x_i^{'}$ wherein attenuation is in basis $e_1^{'}$ and $e_2^{'}$ directions. By multiplying $\lambda_i(x^{'}{}_i)$ to both side of Equation A.7b and integrating voigt format of material damping, Equation A.7 can be rewritten as:

$$div(\overline{\boldsymbol{\sigma}}\widetilde{\boldsymbol{\Lambda}}) = -\omega^2 \rho[\lambda_1(x_1^{'}), \lambda_2(x_2^{'})]\overline{\mathbf{u}} \tag{A.8a}$$

$$\overline{\boldsymbol{\sigma}} = (1 + 2ia_0\xi)\,\mathbf{C}\bar{\boldsymbol{\varepsilon}} \tag{A.8b}$$

$$\overline{\boldsymbol{\varepsilon}} = \frac{1}{2}[(grad\overline{\mathbf{u}})\boldsymbol{\Lambda} + \boldsymbol{\Lambda}^{\boldsymbol{T}}(grad\overline{\mathbf{u}})^T] \tag{A.8c}$$

where ξ is a damping ratio and $a_0 = k_s b$ is non-dimensional frequency, where b is a characteristic length of the physical problem and $k_s = \omega/c_s$ with $c_s = \sqrt{(\mu/\rho)}$, the S-wave speed. $\widetilde{\Lambda}, \Lambda$ are defined as:

$$\tilde{\Lambda}_{ij} = Q_{ik}\tilde{\Lambda}^{'}_{kl}Q_{jl} \tag{A.9}$$

$$\Lambda_{ij} = Q_{ik}\Lambda^{'}{}_{kl}Q_{jl} \tag{A.10}$$

Appendix A (Continued)

$$Q_{ij} = e_i \cdot e_j{}' \tag{A.11}$$

where $\widetilde{\Lambda}' := diag(\lambda_2(x'_2)\lambda_1(x'_1))$ and $\widetilde{\Lambda} = diag(\frac{1}{\lambda_1(x'_1)}, \frac{1}{\lambda_2(x'_2)})$.

Although there is no exact technique suggested in the literature for choosing the stretching function, the proper choices of λ_i lead to the attenuated wave solutions in the direction of propagation. When the inverse Fourier transform is essential to obtain time domain equation, it is suitable to choose the stretching function λ as a simple function of ω [46]:

$$\lambda_i\left(x'_i\right) := \left[1 + {f_i}^e\left(x'_i\right)\right] - i\frac{{f_i}^p\left(x'_i\right)}{k_s} \tag{A.12}$$

where the functions ${f_i}^e, {f_i}^p$ tend to attenuate evanescent and propagating waves, respectively. By choosing stretching function as Equation A.12, $\widetilde{\Lambda}, \Lambda$ can be rewritten as

$$\tilde{\Lambda}_{ij} = \tilde{F}^e_{ij} + \frac{1}{i\omega}\tilde{F}^p_{ij} \tag{A.13}$$

$$\Lambda_{ij} = \frac{1}{({F^e}_{ij} + \frac{1}{i\omega}{F^p}_{ij})} \tag{A.14}$$

where

$$\widetilde{F}^e_{ij} = Q_{ik}\widetilde{F}^{e'}_{kl}Q_{jl} \quad ; \quad \widetilde{F}^p_{ij} = Q_{ik}\widetilde{F}^{p'}_{kl}Q_{jl} \tag{A.15}$$

$${F^e}_{ij} = Q_{ik}{F^{e'}}_{kl}Q_{jl} \quad ; \quad {F^p}_{ij} = Q_{ik}{F^{p'}}_{kl}Q_{jl} \tag{A.16}$$

Appendix A (Continued)

with

$$\widetilde{\mathbf{F}}^{e'} = \mathbf{I} + diag(f_2{}^e\left(x'_2\right), f_1{}^e\left(x'_1\right)) \tag{A.17a}$$

$$\widetilde{\mathbf{F}}^{p'} = c_s \times diag(f_2{}^p\left(x'_2\right), f_1{}^p\left(x'_1\right)) \tag{A.17b}$$

$$\mathbf{F}^{e'} = \mathbf{I} + diag(f_1{}^e\left(x'_1\right), f_2{}^e\left(x'_2\right)) \tag{A.18a}$$

$$\mathbf{F}^{p'} = c_s \times diag(f_1{}^p\left(x'_1\right), f_2{}^p\left(x'_2\right)) \tag{A.18b}$$

The time-domain equation for PML is derived by premultiplying $i\omega\Lambda^{-1}$ and postmultiplying Λ^{-1} into Equation A.8c, substituting Equation A.12, Equation A.13 and Equation A.14 into Equation A.8 and applying the inverse Fourier transform to the resultant:

$$div\left(\boldsymbol{\sigma}\widetilde{\mathbf{F}}^e + \boldsymbol{\Sigma}\widetilde{\mathbf{F}}^p\right) = \rho f_m \ddot{\mathbf{u}} + \rho c_s f_c \dot{\mathbf{u}} + \mu f_k \mathbf{u} \tag{A.19}$$

$$\boldsymbol{\sigma} = \mathbf{C}(\boldsymbol{\varepsilon} + \frac{2\xi b}{c_s}\dot{\boldsymbol{\varepsilon}}) \tag{A.20}$$

$$\begin{aligned}&\mathbf{F}^{eT}\dot{\boldsymbol{\varepsilon}}\mathbf{F}^e + \left(\mathbf{F}^{pT}\boldsymbol{\varepsilon}\mathbf{F}^e + \mathbf{F}^{eT}\boldsymbol{\varepsilon}\mathbf{F}^p\right) + \mathbf{F}^{pT}\mathbf{E}\mathbf{F}^p = \\ &1/2[\mathbf{F}^{pT}(grad\mathbf{u}) + (grad\mathbf{u})^T\mathbf{F}^p] + 1/2[\mathbf{F}^{eT}(grad\dot{\mathbf{u}}) + (grad\dot{\mathbf{u}})^T\mathbf{F}^e]\end{aligned} \tag{A.21}$$

where

$$f_m := \left[1 + f_1{}^e\left(x'_1\right)\right]\left[1 + f_2{}^e\left(x'_2\right)\right]$$

Appendix A (Continued)

$$f_c := \left[1 + {f_1}^e\left(x'_1\right)\right] {f_2}^p\left(x'_2\right) + [1 + {f_2}^e\left(x'_2\right)]{f_1}^p\left(x'_1\right) \tag{A.22}$$

$$f_k := {f_1}^p\left(x'_1\right) {f_2}^p\left(x'_2\right)$$

and

$$\sum := \int_0^t \boldsymbol{\sigma} d\tau \quad ; \quad \mathbf{E} := \int_0^t \boldsymbol{\varepsilon} d\tau \tag{A.23}$$

$$\begin{cases} \overline{\boldsymbol{\sigma}} = 0 & \text{if } \omega = 0 \\ \overline{\boldsymbol{\varepsilon}} = 0 & \text{if } \omega = 0 \end{cases} \tag{A.24}$$

To create a weak form of the problem, Equation A.19 is multiplied by an arbitrary weighting function and integrated over the domain; by balancing the derivatives which is accomplished by integration by parts and applying divergence theorem, we obtain

$$\int_\Omega \rho f_m \mathbf{w}\cdot\ddot{\mathbf{u}} d\Omega + \int_\Omega \rho c_s f_c \mathbf{w}\cdot\dot{\mathbf{u}} d\Omega + \int_\Omega \mu f_c \mathbf{w}\cdot\mathbf{u} d\Omega + \int_\Omega \widetilde{\boldsymbol{\varepsilon}}^e : \boldsymbol{\sigma} d\Omega + \int_\Omega \widetilde{\boldsymbol{\varepsilon}}^p : \boldsymbol{\Sigma} d\Omega = \int_\Gamma \mathbf{w}\cdot(\boldsymbol{\sigma}\widetilde{\mathbf{F}}^e + \boldsymbol{\Sigma}\widetilde{\mathbf{F}}^p)\mathbf{n} d\Gamma \tag{A.25}$$

where $\mathbf{n}$ is a unit normal and $\Gamma = \partial\Omega$ is the boundary of Ω.

Element-wise computations of $\mathbf{w}$ and $\mathbf{u}$ in terms of nodal quantities using proper shape functions lead to a system of equation of motion:

$$\mathbf{m}\ddot{\mathbf{d}} + \mathbf{c}\dot{\mathbf{d}} + \mathbf{k}\mathbf{d} + \mathbf{p}_{\text{int}} = \mathbf{p}_{ext} \tag{A.26}$$

Appendix A (Continued)

where, $\mathbf{p}_{\text{int}}, \mathbf{p}_{ext}$ are an internal forces and external forces respectively. **m, k** and **c** are the mass, stiffness and damping matrices, which can be interpolated in terms of IJth nodal submatrices as:

$$\mathbf{m}^e{}_{IJ} = \int_{\Omega^e} \rho f_m N_I N_J d\Omega \mathbf{I} \tag{A.27a}$$

$$\mathbf{k}^e{}_{IJ} = \int_{\Omega^e} \rho f_k N_I N_J d\Omega \mathbf{I} \tag{A.27b}$$

$$\mathbf{c}^e{}_{IJ} = \int_{\Omega^e} \rho c_s f_c N_I N_J d\Omega \mathbf{I} \tag{A.27c}$$

The element-level internal force term is given by:

$$\mathbf{P}^e = \int_{\Omega^e} \tilde{\mathbf{B}}^{e^T} \hat{\boldsymbol{\sigma}} d\Omega + \int_{\Omega^e} \tilde{\mathbf{B}}^{p^T} \hat{\boldsymbol{\Sigma}} d\Omega \tag{A.28}$$

$\hat{\boldsymbol{\sigma}}$ is a Voigt form of stress

$$\hat{\sigma} = \begin{Bmatrix} \sigma_{11} \\ \sigma_{22} \\ \sigma_{12} \end{Bmatrix} \tag{A.29}$$

$\tilde{\mathbf{B}}^{e^T}$ and $\tilde{\mathbf{B}}^{p^T}$ are defined as:

$$\tilde{\mathbf{B}}^e_I := \begin{bmatrix} \tilde{N}^e_{I1} & 0 \\ 0 & \tilde{N}^e_{I2} \\ \tilde{N}^e_{I2} & \tilde{N}^e_{I1} \end{bmatrix} \quad ; \quad \tilde{\mathbf{B}}^p_I := \begin{bmatrix} \tilde{N}^p_{I1} & 0 \\ 0 & \tilde{N}^p_{I2} \\ \tilde{N}^p_{I2} & \tilde{N}^p_{I1} \end{bmatrix} \tag{A.30}$$

Appendix A (Continued)

with

$$\tilde{N}^e_{Ii} := \tilde{F}^e_{ij} N_{I,j} \quad ; \quad \tilde{N}^p_{Ii} := \tilde{F}^p_{ij} N_{I,j} \tag{A.31}$$

Solution of Equation A.26 requires a time-stepping algorithm such as the Newmark method and the Newton-Raphson to compel the equilibrium. If Equation A.26 is solved at time step t_{n+1} using the solution at t_n, the Newton-Raphson iteration at this time will need the calculation of $\boldsymbol{\sigma}_{n+1}$ and $\boldsymbol{\Sigma}_{n+1}$ in order to compute $\mathbf{p}^e_{n+1}$ and consistent linearization $\mathbf{p}^e_{n+1}$ at $\mathbf{d}^e_{n+1}$, where $\mathbf{d}^e$ is an element-level nodal displacement. Therefore in order to calculate $\tilde{\boldsymbol{\varepsilon}}_{n+1}$, these assumptions

$$\dot{\boldsymbol{\varepsilon}}\left(t_{n+1}\right) \approx \frac{\boldsymbol{\varepsilon}_{n+1} - \boldsymbol{\varepsilon}_n}{\Delta t} \quad ; \quad \mathbf{E}\left(t_{n+1}\right) \approx \mathbf{E}_n + \boldsymbol{\varepsilon}_{n+1}\Delta t \tag{A.32}$$

are considered and substituted into Equation A.19 to obtain

$$\hat{\boldsymbol{\varepsilon}}_{n+1} = \frac{1}{\Delta t}[\mathbf{B}^{\varepsilon}\boldsymbol{\upsilon}_{n+1} + \mathbf{B}^{\varrho}\boldsymbol{\upsilon}_{n+1} + \frac{1}{\Delta t}\hat{\mathbf{F}}^{\varepsilon}\hat{\boldsymbol{\varepsilon}}_n - \hat{\mathbf{F}}^{\varrho}\hat{\mathbf{E}}_n] \tag{A.33}$$

$$\mathbf{F}^{\iota} := \left[\frac{\mathbf{F}^e}{\Delta t} + \mathbf{F}^p\right]^{-1} \quad ; \quad \mathbf{F}^{\varepsilon} := \mathbf{F}^e\mathbf{F}^{\iota} \quad , \mathbf{F}^{\varrho} := \mathbf{F}^p\mathbf{F}^{\iota} \quad ; \quad \hat{\boldsymbol{\varepsilon}} := \left\{ \begin{array}{c} \varepsilon_{11} \\ \varepsilon_{22} \\ 2\varepsilon_{12} \end{array} \right\} \tag{A.34}$$

Appendix A (Continued)

where $\hat{\mathbf{E}}$ is the time-integral of $\hat{\boldsymbol{\varepsilon}}$. With

$$\mathbf{B}_I{}^{\varepsilon} := \begin{bmatrix} F^{\varepsilon}_{11}N^{\iota}_{I1} & F^{\varepsilon}_{21}N^{\iota}_{I1} \\ F^{\varepsilon}_{12}N^{\iota}_{I2} & F^{\varepsilon}_{22}N^{\iota}_{I2} \\ F^{\varepsilon}_{11}N^{\iota}_{I2} + F^{\varepsilon}_{12}N^{\iota}_{I1} & F^{\varepsilon}_{21}N^{\iota}_{I2} + F^{\varepsilon}_{22}N^{\iota}_{I1} \end{bmatrix} \tag{A.35}$$

$$\mathbf{B}_I{}^{\varrho} := \begin{bmatrix} F^{\varrho}_{11}N^{\iota}_{I1} & F^{\varrho}_{21}N^{\iota}_{I1} \\ F^{\varrho}_{12}N^{\iota}_{I2} & F^{\varrho}_{22}N^{\iota}_{I2} \\ F^{\varrho}_{11}N^{\iota}_{I2} + F^{\varrho}_{12}N^{\iota}_{I1} & F^{\varrho}_{21}N^{\iota}_{I2} + F^{\varrho}_{22}N^{\iota}_{I1} \end{bmatrix}$$

where $N^{\iota}_{Ii} := F^{\iota}_{ij}N_{I,j}$ and

$$\hat{\mathbf{F}}^{\varepsilon} := \begin{bmatrix} (F^{\varepsilon}_{11})^2 & (F^{\varepsilon}_{21})^2 & F^{\varepsilon}_{11}F^{\varepsilon}_{21} \\ (F^{\varepsilon}_{12})^2 & (F^{\varepsilon}_{22})^2 & F^{\varepsilon}_{12}F^{\varepsilon}_{22} \\ 2F^{\varepsilon}_{11}F^{\varepsilon}_{12} & 2F^{\varepsilon}_{21}F^{\varepsilon}_{22} & F^{\varepsilon}_{11}F^{\varepsilon}_{22} + F^{\varepsilon}_{12}F^{\varepsilon}_{21} \end{bmatrix} \tag{A.36}$$

$$\hat{\mathbf{F}}^{\varrho} := \begin{bmatrix} (F^{\varrho}_{11})^2 & (F^{\varrho}_{21})^2 & F^{\varrho}_{11}F^{\varrho}_{21} \\ (F^{\varrho}_{12})^2 & (F^{\varrho}_{22})^2 & F^{\varrho}_{12}F^{\varrho}_{22} \\ 2F^{\varrho}_{11}F^{\varrho}_{12} & 2F^{\varrho}_{21}F^{\varrho}_{22} & F^{\varrho}_{11}F^{\varrho}_{22} + F^{\varrho}_{12}F^{\varrho}_{21} \end{bmatrix}$$

$\hat{\boldsymbol{\sigma}}_{n+1}$ is computed using Equation A.32 and Equation A.19.

$$\hat{\boldsymbol{\sigma}}_{n+1} = \left(1 + \frac{2\xi b}{c_s \Delta t}\right)\mathbf{D}\hat{\boldsymbol{\varepsilon}}_{n+1} - \frac{2\xi b}{c_s \Delta t}\mathbf{D}\hat{\boldsymbol{\varepsilon}}_n \tag{A.37}$$

Appendix A (Continued)

If

$$\hat{\mathbf{\Sigma}}_{n+1} = \hat{\mathbf{\Sigma}}_n + \hat{\boldsymbol{\sigma}}_{n+1}\Delta t \tag{A.38}$$

By substituting of Equation A.38 into Equation A.27b, we obtain

$$\mathbf{p^e_{n+1}} = \int_{\Omega^e} \tilde{\mathbf{B}}^T \hat{\boldsymbol{\sigma}}_{n+1} d\Omega + \int_{\Omega^e} \tilde{\mathbf{B}}^{p^T} \hat{\mathbf{\Sigma}}_n d\Omega \tag{A.39}$$

where

$$\tilde{\mathbf{B}} := \tilde{\mathbf{B}}^e + \Delta t \tilde{\mathbf{B}}^p \tag{A.40}$$

Equation A.37 and Equation A.33 along with linearization of Equation A.39 give

$$\Delta \mathbf{p}^e_{n+1} = \left[\int_{\Omega^e} \tilde{\mathbf{B}}^T \tilde{\mathbf{D}} \mathbf{B}^{\varepsilon} d\Omega\right] \Delta \boldsymbol{v}_{n+1} + \left[\int_{\Omega^e} \tilde{\mathbf{B}}^T \tilde{\mathbf{D}} \mathbf{B}^{\varrho} d\Omega\right] \Delta \mathbf{d}_{n+1} \tag{A.41}$$

where

$$\tilde{\mathbf{D}} = \frac{1}{\Delta t}\left(1 + \frac{2\xi b}{c_s \Delta t}\right)\mathbf{D} \tag{A.42}$$

and

$$\breve{\mathbf{c}}^e = \left[\int_{\Omega^e} \tilde{\mathbf{B}}^T \tilde{\mathbf{D}} \mathbf{B}^{\varepsilon} d\Omega\right] \quad ; \quad \breve{\mathbf{k}}^e = \left[\int_{\Omega^e} \tilde{\mathbf{B}}^T \tilde{\mathbf{D}} \mathbf{B}^{\varrho} d\Omega\right] \tag{A.43}$$

Equation A.43 is an essential part of effective tangent stiffness matrix and should be integrated into the time-stepping algorithm.

Appendix A

COPYRIGHT PERMISSIONS

Title: Efficient computation of wave propagation along axisymmetric pipes under non-axisymmetric loading

Author: Zahra Heidary,Didem Ozevin

Publication: Finite Elements in Analysis and Design

Publisher: Elsevier

Date: 1 September 2014

Logged in as: Zahra Heidary

UIC

Account #: 3000802319

Order Completed

Thank you very much for your order.

This is a License Agreement between UIC – Zahra Heidary ("You") and Elsevier ("Elsevier"). The license consists of your order details, the terms and conditions provided by Elsevier, and the payment terms and conditions.

Get the printable license.

License Number

3502011038209

Appendix A (Continued)

License date

Nov 04, 2014

Licensed content publisher

Elsevier

Licensed content publication: Finite Elements in Analysis and Design

Licensed content title: Efficient computation of wave propagation along axisymmetric pipes under non-axisymmetric loading

Licensed content author: Zahra Heidary,Didem Ozevin

Licensed content date: 1 September 2014

Licensed content volume number: 86

Licensed content issue number: n/a

Number of pages: 8

Type of Use: reuse in a thesis/dissertation

Portion: full article

Format: both print and electronic

Are you the author of this Elsevier article? Yes

Will you be translating? No

Title of your thesis/dissertation: Numerical Modeling of Wave Propagation at Large Scale Damaged Structures For Quantitative AE

Expected completion date: Nov 2014

Estimated size (number of pages): 130

Appendix A (Continued)

Elsevier VAT number: GB 494 6272 12

Permissions price: 0.00 USD

VAT/Local Sales Tax: 0.00 USD / 0.00 GBP

Total: 0.00 USD

Thank you for seeking permission from SPIE to reprint material from our publications. As author, SPIE shares the copyright with you, so you retain the right to reproduce your paper in part or in whole.

Publisher's permission is hereby granted under the following conditions:

(1) the material to be used has appeared in our publication without credit or acknowledgment to another source; and

(2) you credit the original SPIE publication. Include the authors' names, title of paper, volume title, SPIE volume number, and year of publication in your credit statement.

Sincerely,

Karen Thomas for

Eric Pepper, Director of Publications

SPIE

P.O. Box 10, Bellingham WA 98227-0010 USA

360/676-3290 (Pacific Time) eric@spie.org

CITED LITERATURE

1. Heidary, Z. and Ozevin, D.: The selection of spectral element polynomial orders for high frequency numerical wave propagation. In Nondestructive Characterization for Composite Materials Aerospace Engineering Civil Infrastructure and Homeland Security 2013, eds. T. Y. Yu, A. L. Gyekenyesi, P. J. Shull, A. A. Diaz, H. F. Wu, and A. E. Aktan, page 86941F, April 2013.

2. Heidary, Z. and Ozevin, D.: High frequency elastic wave propagation in large structures using spectral elements and perfectly matched layer. In Nondestructive Characterization for Composite Materials Aerospace Engineering Civil Infrastructure and Homeland Security 2014, eds. H. F. Wu, T.-Y. Yu, A. L. Gyekenyesi, and P. J. Shull, page 906309, March 2014.

3. Heidary, Z. and Ozevin, D.: Efficient computation of wave propagation along axisymmetric pipes under non-axisymmetric loading. Finite Elements in Analysis and Design, 86:81–88, September 2014.

4. Prosser, W. H., Hamstad, M. A., Gary, J., and Gallagher, A.: Finite Element and Plate Theory Modeling of Acoustic Emission Waveforms. Journal of Nondestructive Evaluation, 18(3):83–90, 1999.

5. Graff, K.F. : Wave Motion in Elastic Solids. Dover Publications Inc, 1991.

6. Liu, M., Frabgopol, D., and Kim, S.: Bridge System Performance Assessment from Structural Health Monitoring: A Case Study. Journal of Structural Engineering, 135:733–742, 2009.

7. Benedetti, M., Fontanari, v., and Zonta, D.: Structural Health Monitoring of Wind Towers: Remote Damage Detection using Strain Sensors. Smart Materials and Structures, 20:055009, 2011.

8. Pakzad, S. and Fenves, G.: Structural Health Monitoring of Wind Towers: Remote Damage Detection using Strain Sensors. Journal of Structural Engineering, 135:863–872, 2009.

9. Sung, S. H., Park, J. W., Nagaama, T., and Jung, H. J.: A multi-scale sensing and diagnosis syste, combining accelerometers and gyroscopes for bridge health monitoring. Smart Materials and Structures, 23:015005, 2014.

10. Johnson, M., Ozevin, D., Washer, G., Ono, K., Gostautas, R., and Tamutus, T.: A multi-scale sensing and diagnosis syste, combining accelerometers and gyroscopes for bridge health monitoring. Journal of Transportation Research Board, 2313:72–79, 2012.

11. Leone, F. A., Ozevin, D., Awerbuch, J., and Tan, T. M.: Detecting and Locating Damage Initiation and Progression in Full-Scale Sandwich Composite Fuselage Panels using Acoustic Emission. Journal of Composite Materials, 47:1643–1664, 2013.

12. Chang, P. and Flatau, A. L. S.: Review Paper: Health Monitoring of Civil Infrastructure. International Journal of Structural Health Monitoring, 2(2):257–267, 2003.

13. Stephens, R. W. B. and Pollock, A. A.: Waveforms and Frequency Spectra of Acoustic Emissions. Journal of the Acoustical Society of America, 50(3):904–910, 1971.

14. Grosse, C. U. and Ohtsu, M.: Acoustic Emission Testing: Basics for Research-Applications in Civil Engineering. Springer, 2008.

15. Sung, D. U., Oh, J. H., Kim, C. G., and Hong, C. S.: Impact Monitoring of Smart Composite Laminates Using Neural Network and Wavelet Analysis. Journal of Intelligent Material Systems and Structures, 11:180–190, 2000.

16. Bhat, C.and Bhat, M. and Murthy, C. R. L.: Characterization of Failure Modes in CFRP Composites An ANN Approach. Journal of Composite Materials, 42:257–276, 2008.

17. Kostopoulos, V.and Loutas, T. H., Kontsos, A.and Sotiriadis, G., and Pappas, Y. Z.: On the Identification of the Failure Mechanisms in Oxide/oxide Composites using Acoustic Emission. NDT and E International, 36:571–580, 2003.

18. Ativitavas, N., Pothisiri, T., and Fowler, T. J.: Identification of Fiber-reinforced Plastic Failure Mechanisms from Acoustic Emission Data using Neural Networks. Journal of Composite Materials, 40:193–226, 2006.

19. Mal, A.; Banerjee, S. and Ricci, F.: An automated damage identification technique based on vibration and wave propagation data. Philosophical Transactions of the Royal Society A, 365:479–491, 2007.

20. Marec, A., Thomas, J., and Guerjouma, R. E.: Damage characterization of polymer-based composite materials: Multivariable analysis and wavelet transform for clustering acoustic emission data. Mechanical Systems and Signal Processing, 22:1441–1464, 2008.

21. Oliveira, R. D. and Marques, A. T.: Identification of Fiber-reinforced Plastic Failure Mechanisms from Acoustic Emission Data using Neural Networks. Computers and Structures, 86:367–373, 2008.

22. Santis, S. D. and Tomor, A. K.: Laboratory and Field Studies on the use of Acoustic Emission for Masonry Bridges. NDT and E International, 55:64–74, 2013.

23. Bellenger, F.; Mazille, H. and Idrissi, H.: Use of acoustic emission technique for the early detection of aluminum alloys exfoliation corrosion. NDT and E International, 35:385–392, 2002.

24. Yu, J. and Ziehl, P.: Stable and unstable fatigue prediction for A572 structural steel using acoustic emission. Journal of Constructional Steel Research, 77:173–179, 2012.

25. De Basabe, J. D. and Sen, M. K.: On some properties of 2D spectral finite elements in problems of wave propagation. Geophysics, 72:T81–T95, 2007.

26. Mattsson, K. and Nordstrom, J.: High order finite difference methods for wave propagation in discontinuous media. Journal of Computational Physics, 220:249–269, 2006.

27. Dominguez, J.: Boundary elements in dynamics. Computational Mechanics Publications, 1993.

28. Ling, X. and Cherukuri, H. P.: Stability Analysis of an Explicit Finite Element Scheme for Plane Wave Motions in Elastic Solids. Computational Mechanics, 29:430–440, 2002.

29. Hill, R., Forsyth, S., and Macey, P.: Finite element modelling of ultrasound, with reference to transducers and AE waves. Ultrasonics, 42(1-9):253–8, April 2004.

30. Patera, A. T.: A spectral element method for fluid dynamics: laminar flow in a channel expansion. Journal of Computational Physics, 54:468–488, 1984.

31. Doyle, J. F.: Wave propagation in structures. Springer, 1989.

32. Krawczuk, M., Palacz, M., and Ostachowicz, W.: The dynamic analysis of cracked Timoshenko beam by the spectral element method. Journal of Sound and Vibration, 264:11391153, 2003.

33. Pozrikidis, C.: Introduction to Finite and Spectral Element Methods Using MATLAB. Chapman and Hall/CRC, 2005.

34. Kudela, P. and Ostachowicz, W.: 3D time-domain spectral element for stress waves modeling. Proceeding of the 7th International Conference on Modern Practice in Stress and Vibration Analysis, 181, 2009.

35. Kudela, P., Krawczuk, M., and Ostachowicz, W.: Wave propagation modeling in 1D structures using spectral element method. Journal of Sound and Vibration, 300:88–100, 2007.

36. Zak, A., Krawczuk, M., and Ostachowicz, W.: Wave propagation modeling in 1D structures using spectral element method. Finite Elements in Analysis and Design, 42:929–941, 2006.

37. Zak, A., Krawczuk, M., and Ostachowicz, W.: Certain numerical issue of wave propagation modeling in rods by the Spectral Finite Element Method. Finite Elements in Analysis and Design, 47:1036–1046, 2011.

38. Kim, Y., Ha, S., and Chang, F. K.: Time-domain spectral element method for built-in piezoelectric actuator-induced lamb wave propagation analysis. AIAA Journal, 46:591–600, 2008.

39. Witkowski, W., Rucka, M., Chroirlrwski, J., and Wilde, K.: On some properties of 2D spectral finite elements in problems of wave propagation. Finite Elements in Analysis and Design, 55:31–41, 2012.

40. Peng, H., Meng, G., and Li, F.: Modeling of wave propagation in plate structures using three-dimensional spectral element method for damage detection. Journal of Sound and Vibration, 320(4-5):942–954, March 2009.

41. Mehdizadeh, O. Z. and Paraschivoiu, M.: Investigation of a two dimensional spectral element method for Helmholtzs equation. Journal of Computational Physics, 189:111–129, 2003.

42. Achenbach, J. D.: Wave Propagation in Elastic Solids. American Elsevier Publishing Company, Inc - New York, 1973.

43. Kucukcoban, S. and Kallivokas, L.: Mixed perfectly-matched-layers for direct transient analysis in 2D elastic heterogeneous media. Computer Methods in Applied Mechanics and Engineering, 200(1-4):57–76, January 2011.

44. Komatitsch, D. and Tromp, J.: A perfectly matched layer absorbing boundary condition for the second-order seismic wave equation. Geophysical Journal International, 154(1):146–153, July 2003.

45. Tsynkov, S. V.: Numerical solution of problems on unbounded domains. A review. Applied Numerical Mathematics, 27:465–532, 1998.

46. Festa, G. and Vilotte, J. P.: The Newmark scheme as velocity-stress time-staggering: an efficient PML implementation for spectral element simulations of elastodynamics. Geophysical Journal International, 161(3):789–812, June 2005.

47. Cerjan, C., Kosloff, D., Kosloff, R., and Reshef, M.: nonreflecting boundary condition for discrete acoustic and elastic wave equation. Geophysics, 50:705–708, 1985.

48. Sochacki, J., Kubichek, R., George, J., Fletcher, W. R., and Smithson, S.: Absorbing boundary conditions and surface waves. Geophysics, 52:60–71, 1987.

49. Peng, C. and Toksoz, M. N.: An optimal absorbing boundary condition for elastic wave modeling. Geophysics, 60:269–301, 1995.

50. Clayton, R. and ENGQUIST, B.: Absorbing boundary conditions for acoustic and elastic wave equations. Seismological Society of America, 6:1529–1540, 1977.

51. Brenger, J. P.: A perfectly matched layer for the absorption of electromagnetic waves. Journal of Computational Physics, 114:185200, 1994.

52. Brenger, J. P.: Three-dimensional perfectly matched layer for the absorption of electromagnetic waves. Journal of Computational Physics, 127:363379, 1996.

53. Abarbanel, S. and Gottlieb, D.: A Mathematical Analysis of the PML Method. Journal of Computational Physics, 134:357–363, 1997.

54. Chew, W. C. and Weedon, W. H.: A 3D perfectly matched medium from modified Maxwells equations with stretched coordinates. Microwave and Optical Technology Letters, 7:599–604, 1994.

55. Wang, T. and Tang, X.: Finite-difference modeling of elastic wave propagation: a nonsplitting perfectly matched layer approach. Geophysics, 68:1749–1755, 2003.

56. Basu, U. and Chopra, A. K.: Perfectly matched layers for time-harmonic elastodynamics of unbounded domains: theory and finite-element implementation. 192(11-12):1337–1375, March 2003.

57. Basu, U. and Chopra, A. K.: Perfectly matched layers for transient elastodynamics of unbounded domains. International Journal for Numerical Methods in Engineering, 59(8):1039–1074, February 2004.

58. Dahlquist, G. and Bjorck, A.: Numerical Methods. Dover Publications Inc., 2003.

59. Bathe, K. J.: Finite Element Procedures. Prentice Hall, Pearson Education Inc., 1995.

60. Rose, J. L., Jiao, D., and Spanner, J.: Ultrasonic guided wave NDE for piping. Materials Evaluation, 54:1310–1313, 1996.

61. Kirby, R., Zletev, Z., and Mudge, P.: On the scattering of torsional waves from axisymmetric defects in coated pipes. Journal of Sound and Vibration, 31:3989–4004, 2012.

62. Juliano, T. M. ; Meegoda, J. N. and Watts, D. J.: Acoustic emission leak detection on a metal pipeline buried in sandy soil. Journal of Pipeline Systems Engineering and Practice, 4:149–155, 2013.

63. Miller, R. K., Pollock, A., Watts, D., Carlyle, J. M., Tafure, A. N., and Yezzi, J. J.: A reference standard for the development of acoustic emission pipeline leak detection technique. NDT and E International, 32:1–8, 1999.

64. Khulief, Y. A., Khalifa, A., Mansour, R. B., and Habib, M. A.: Acoustic detection of leaks in water pipelines using measurements inside pipe. Journal of Pipeline Systems Engineering and Practice, 3:47–54, 2011.

65. Balk, K., Jiang, J., and Leighton, T. G.: Acoustic attenuation, phase and group velocities in liquid-filled pipes III: Nonaxisymmetric propagation and circumferential modes in lossless conditions. Journal of the Acoustical Society of America, 133:1225–1236, 2013.

66. Qing-tian, D. and Zhi-chun, Y.: Wave propagation analysis in buried pipe conveying fluid. Applied Mathematical Modeling, 37:6225–6233, 2013.

67. Shehadeh, M. F., Abdou, W., Steel, J. A., and Reuben, R.: Aspects of acoustic emission attenuation in steel pipes subject to different internal and external environments. Journal of Process Mechanical Engineering, 222:41–54, 2007.

68. Nishino, H., Yoshida, K., Cho, H., and Takemoto, M.: Propagation phenomena of wideband guided waves in a bended pipe. Ultrasonics, 44:1139–1143, 2006.

69. Na, W. B. and Kundu, T.: Wave attenuation in pipes and its application in determining axial spacing of monitoring sensors, Materials Evaluation. Materials Evaluation, pages 635–644, 2002.

70. Luo, W.: Ultrasonic guided waves in wave scattering in viscoelastic coated hollow cylinders. Ph.D. dissertation, The Pennsylvania State University, 2005.

71. Gazis, D. C.: Three-dimensional investigation of the propagation of waves in hollow circular cylinders I analytical foundation. Journal of the Acoustical Society of America, 31:568–573, 1959.

72. Zhuang, W., Shah, A. H., and Dong, S. B.: Elastodynamic Greens functions for laminated anisotropic circular cylinders. Journal of Applied Mechanics, pages 665–674, 1999.

73. Bai, H., Taciroglu, E., Dong, S. B., and Shah, A. H.: Elastodynamic Greens functions for laminated piezoelectric cylinder. International Journal of Solids and Structures, pages 6335–6350, 2004.

74. Zhou, W. J., Inchchou, M. N., and Mencik, J. M.: Analysis of wave propagation in cylindrical pipes with local inhomogeneities. Journal of Sound and Vibration, 319:335–354, 2009.

75. Mazzotti, M., Marzani, A., Bartoli, I., and Viola, E.: Guided waves dispersion analysis for prestressed viscoelastic waveguides by means of the SAFE method. International Journal of Solids and Structures, 49:2359–2372, 2012.

76. Gsell, D., Leutengger, T., and Dual, J.: Modeling three-dimensional elastic wave propagation in circular cylindrical structures using a finite-difference approach. Journal of the Acoustical Society of America, 116:3284–3293, 2003.

77. Zienkiewicz, O. C. and Talor, R. L.: The finite element method for Solid and Structural Mechanics. Butterworth-Heinemann Inc, 2000.

78. Nagarajan, S. and Popov, E.: Elastic-plastic dynamic analysis solids of axisymmetric solids. Computers and Structures, 4:1117–1134, 1974.

79. Wilson, E. L.: Structural analysis of axisymmetric solids. AIAA Journal, 3:2269–2274, 1965.

80. Ladefoged, T.: Triangular ring element with analytic expressions for stiffness and mass matrix. Computer Methods in Applied Mechanics and Engineering, 67:171–187, 1988.

81. Wunderlich, W., Cramer, H., and Obrecht, H.: Application of ring elements in the nonlinear analysis of shells of revolution under nonaxisymmetric loading. Computer Methods in Applied Mechanics and Engineering, pages 259–275, 1985.

82. Bouzid, D. A., Tiliouine, B., and Vermeer, P. A.: Exact formulation of interface stiffness matrix for axisymmetric bodies under non-axisymmetric loading. Computers and Geotechnics, 31:75–87, 2004.

83. Cook, R. D., Malkus, D. S., and Plesha, M. E.: Concepts and Applications of Finite Element Analysis. Wiley and Sons Inc., 1989.

84. Hoskins, R. F.: Delta Function: An Introduction to Generalised Functions. Horwood Publishing limited, 1999.

85. Rao, S. S.: Vibration of Continuous Systems. John Wiley and Sons Inc, 2007.

86. Marzani, A.: Time-transient response for ultrasonic guided waves propagating in damped cylinders. International Journal of Solids and Structures, 45:6347–6368, 2008.

87. Goldsmith, W.: Impact: The Theory and Physical Behavior of Colliding Solids. Dover Publications, 2001.

88. Giurgiutiu, V.: Structural Health Monitoring with Piezoelectric Wafer Active Sensors. Academic Press, 2008.

89. Sause, M. G. R. and Hamstad, M. A.: Ultrasonic guided wave NDE for piping. Sensors and Actuators A: Physical, 184:64–71, 2012.

90. Sause, M. G. R. and Horn, S.: Simulation of Acoustic Emission in Planar Carbon Fiber Reinforced Plastic Specimens. Journal of Nondestructive Evaluation, 29:123142, 2010.

91. Agrawal, A. and Sharma, A.: Perfectly matched layer in numerical wave propagation: factors that affect its performance. Applied optics, 43:4225–4231, 2004.

VITA

Zahra Heidary

zheida2@uic.edu

EDUCATION

2014 University of Illinois at Chicago, Chicago, IL

Ph.D. in Civil Engineering,

Thesis: Numerical Modeling of Wave Propagation at Large Scale Damaged Structures for Quantitative Acoustic Emission

2005 University of Shahid Bahonar, Iran

Bachelor of Science in Mathematics,

EXPERIENCE

Research Assistant, September 2012 December 2014

University of Illinois at Chicago, Chicago, IL

- Developed multiphysics models of structural and piezoelectric physics for quantitative Acoustic Emission (AE) testing;
- Coupled spectral element modeling (SEM) and absorbing boundary condition (ABC) to study elastodynamic problem at large structural systems;
- Developed an efficient formulation of the problem of wave propagation and attenuation along the length of axisymmetric pipes under non-axisymmetric loading such as leaks

or new cracks in order to calculate the optimal sensor placement for structural health monitoring (SHM);

- Identified the boundary domain variables for eliminating reflections from sub-domain formulation of the structure;
- Validated the formulation with the conventional approach and an experimental program.

Teaching Assistant, September 2011- May. 2014

- Static;
- Strength of Materials;
- Behavior and Design of Metal Structures;
- Fracture Mechanics.

Structural Engineer, December 2005 December 2010

Moradi Multi Dimensions, Consulting Engineers, Chicago, IL

- Inspected buildings, bridges and porches to determine their physical state and fitness to service;
- Participated in structural design and review of projects including bridges, buildings, platforms and shoring systems;
- Worked with: ANSYS, ABAQUS, AUTOCAD, COMSOL Multiphysics and MATLAB Softwares.

Projects Involved

- Analysis of Acoustic Emission Signals in GlidCop Fatigue Study funded by Argonne National Laboratory (2014);
- Hybrid State-Detection System for Gearbox Component funded by NAVAIR (2013-2014);
- The crack detection in orthotropic bridge decks using Acoustic Emission (2010).

Honors and Awards

- UIC Chancellor's Graduate Research Fellowship for interdisciplinary research (2013-2014);
- UIC Research Forum Competition Award under Life Sciences/Engineering Category (2013);
- Graduate Student Fellowship for NSF CMMI Engineering Research Conference (2012);
- Ranked among top 0.01% of national entry college exam in Iran (2000);
- Selected as one of the national students Mathematics Olympiad test (1997)

Refereed Journal Publications

- Z. Heidary, D. Ozevin, The Selection of Polynomial Order and Element Size for the Spectral Element Formulation of High Frequency Elastic Wave Equation Journal of Sound and Vibration, in preparation.
- Z. Heidary, D. Ozevin, On the Influence of Boundary Reflections to the Characteristics of Elastic Waves for Pattern Recognition Methods, Journal of NDT&E international, submitted.
- Z. Heidary, D. Ozevin, Efficient computation of wave propagation along axisymmetric pipes under non-axisymmetric loading, Journal of Finite Elements in Analysis and Design, Vol. 86, pp.81-88, 2014.

- D. Ozevin, Z. Heidary, Acoustic Emission Source Orientation Based on Time Scale, Journal of Acoustic Emission, Vol. 29, pp. 123-132, 2011.

Conference Publications

- Z. Heidary, D. Ozevin, High Frequency Elastic Wave Propagation in Large Structures using Spectral Elements and Perfectly Matched Layers SPIE NDE/Smart Structures International Conference, March 2014.
- Z. Heidary, D. Ozevin, Damage Quantification using Wave Propagation Data with Integrated Numerical and Experimental Approach, ASME 2013 International Mechanical Engineering Congress & Exposition, November 2013.
- Z. Heidary, D. Ozevin, The Effectiveness of Spectral element Method for High Frequency Wave Propagation SPIE NDE/Smart Structures International Conference, March 2013.
- Z. Heidary, D. Ozevin, H.Yalnkaya, 2D Numerical Modeling of Pipeline Structures with Non- Axisymmetric Loads and Spectral Elements for Identifying Reliable Sensor Spacing International Workshop on Structural Health Monitoring, IWSHM 2013 Stanford, CA., September 2013.
- Z. Heidary, D. Ozevin, Multiphysics Modeling for Quantitative Acoustic Emission Testing of Civil Structures, SPIE NDE/Smart Structures International Conference, March 2012.
- D. Ozevin, Z. Li, Z. Heidary, Early Stage Damage Detection of Aluminum 7075-T6 Plate Based on Acoustic Emission, SPIE NDE/Smart Structures International Conference, March 2011.

TECHNICAL PRESENTATION

Z. Heidary, D. Ozevin Real Time Damage Detection in Structures with Quantification in Acoustic Emission Method and Effective Numerical Formulation, Dalian University of Technology, China, June 2013.

Advanced Courses Taken

Structural Dynamics, Advanced Finite Element, Nonlinear Finite Element, Fracture Mechanics and Failure Analysis, Plasticity, Continuum Mechanics, Characterization of Materials by Nondestructive Testing.

Synergistic Activities

- Certified LabVIEW Associate Developer (CLAD).
- Member of American Society of Civil Engineers (ASCE).
- One of founding member of UIC Department of Civil and Materials Engineering (CME) Graduate Student Association.
- Member of the Society of Women Engineers (SWE).